Sofia University "St. Kl. Ohridski"

Faculty of Physics
Atomic Physics Dept.

Bachelor thesis

Construction and study of a Compton camera for gamma ray measurements

Galin Bistrev

Nuclear and Particle Physics, Faculty number: № 2PH0760003

Supervisor:
Assoc. prof. d-r Venelin Kozhuharov

Sofia, 10 September 2025

Contents

Chapter 1

Introduction

Gamma-ray spectroscopy is a method for identifying and quantifying radionuclides through analysis of the energy and intensity of gamma rays emitted during nuclear transitions from excited to lower energy states. Measurement of the energies and intensities of the produced gamma emissions enables precise characterization of radioactive sources. This method is fundamental in nuclear physics, environmental monitoring, and radiation protection.It also has various applications in medicine and industry, where accurate analysis of radioactive materials is essential. Gamma-ray spectroscopy not only enables detailed analysis of radionuclides but also serves as a powerful tool in astrophysics, revealing high-energy processes in the cosmic environment.

In order to study the gamma-ray spectrum, a suitable detector medium with which the gamma particles can interact must be employed. Interactions within detector produce an electrical signal, which is subsequently processed and analyzed by accompanying electronic components to extract information about the energy and intensity of the radiation. That is the reason why characteristics such as detection efficiency and energy resolution are important, when constructing such detector.

There are various types of detectors used in gamma-ray spectroscopy, each selected based on the specific objectives of the measurement, e.g. accurately determining the energy of incoming gamma photons or reconstructing the direction of origin. The detector which will be a topic of study in this bachelor thesis is the Compton camera.

In the following chapters the principle of operation of the Compton camera is discussed along with applications in various fields. Experimental results are also presented for prototype components of a Compton camera, constructed with two monolithic $CeBr_3$ scintillation crystals of different dimensions, each tested separately by coupling to a single silicon photomultiplier (SiPM). Through analysis of these results the performance and capabilities of the system are evaluated.

Chapter 2

Gamma ray detection

2.1 Interaction of gamma rays with matter

There are number of ways in which gamma rays interact with matter, but in the context of radiation detection and measurement, only three mechanisms are of primary importance. These are the photoelectric effect, Compton scattering, and pair production. Each of those processes involves either a complete absorption or a partial transfer of the photon's energy to the material and is characterized by a specific energy threshold and cross section that depends on many factors including photon energy and the atomic number Z of the material.

In the photoelectric effect process, a photon undergoes an interaction with an absorber atom in which the photon transfers all of its energy to an electron in the shell, which is than emitted with energy:

$$E = h\nu - E_b. \tag{2.1}$$

Here E_b represents the binding energy of the electron in the shell before the interaction. The most probable origin of the photoelectron, given that the incident photon has sufficient energy, is the K shell of the atom. The probability for an photoelectric effect to occur is measured by the cross section of the interaction σ_{ph}. In general it is a function of Z of the target atom and photon's incident energy E_γ [1]:

$$\sigma_{\text{ph}} \propto \frac{Z^4}{E_\gamma^{3.5}}. \tag{2.2}$$

For higher precision in the same energy range ($< 0.5\ MeV$), the Sauter equation [2] is a more appropriate alternative:

$$\sigma_{\text{ph}} = \frac{3}{2}\phi_0\alpha^4 \left(Z\frac{E_e}{E_\gamma}\right)^5 \left(\gamma^2-1\right)^{3/2} \left[\frac{4}{3} + \frac{\gamma(\gamma-2)}{\gamma+1}\left(1 - \frac{1}{2\gamma(\gamma^2-1)^{1/2}} \ln\frac{\gamma+(\gamma^2-1)^{1/2}}{\gamma-(\gamma^2-1)^{1/2}}\right)\right] \tag{2.3}$$

Here

$$\gamma = \frac{E_\gamma - E_b + E_e}{E_e}$$

, ϕ_0 is the Thompson cross section ($\phi_0 \approx 0.66526\ barn$), $E_e = m_e c^2 = 5.11 \times 10^5\ eV$ is the electron's rest energy, and *alpha* is the fine structure constant.

At photon energies above 0.5 MeV, the photoelectric cross section becomes small, as other interactions become more dominant. Thus for precise calculations of the photoelectric effect at high energies, the Pratt–Scofield equation [3][4] is used:

$$\sigma_{\mathrm{ph}} = Z^5 \left(\sum_{n=1}^{4} \frac{a_n + b_n Z}{1 + c_n Z} k^{-p_n} + f_{corr,ph} \right) \tag{2.4}$$

where $k = \frac{E_\gamma}{E_e}$.All the other parameters in the equation are listed in Hubbel [5].

In energy ranges above ∼0.1 MeV, the Compton effect occurs with higher probability compared to the photoelectric effect, becoming the dominant photon interaction mechanism up to several MeV. The process of Compton scattering occurs when an incident gamma ray photon interacts with a bound orbital electron. Since the binding energy of the electron is small compared to the photon's energy, the electron is ejected from the shell. This type of interaction follows the kinematics of a particle–particle scattering event. In this case, the incoming photon collides with an electron, transferring part of its energy. As a result, the photon is deflected and continues in a new direction, forming an angle θ with respect to its original path. The electron, now ejected from the atom, moves away at an angle ϕ relative to the original direction. The formula which relates the energy transfer and the scattering angle is [6]:

$$\cos\theta_C = 1 + m_e c^2 (\frac{1}{E_t} - \frac{1}{E_2}). \tag{2.5}$$

Here

$$E_t = E_1 + E_2$$

is the total energy of the incoming photon, E_1 is the energy of the Compton scattered gamma quant and E_2 is the absorbed energy. The cross section for Compton scattering is evaluated using the integrated form of the Klein–Nishina formula [5]:

$$\sigma_C = Z 2\pi r_e^2 \left\{ \frac{1+k}{k^2} \left[\frac{2(1+k)}{1+2k} - \frac{\ln(1+2k)}{k} \right] + \frac{\ln(1+2k)}{2k} - \frac{1+3k}{(1+2k)^2} + f_{corr,C} \right\} \tag{2.6}$$

For energies lower than 0.1 MeV the above equation is substituted by [5]:

$$\sigma_C = Z \frac{8}{3} \pi r_e^2 \frac{1}{(1+2k)^2} \left(1 + 2k + \frac{6}{5}k^2 - \frac{1}{2}k^3 + \frac{2}{7}k^4 - \frac{6}{35}k^5 + \frac{8}{105}k^6 + \frac{4}{105}k^7 + ... \right) \tag{2.7}$$

At energies of exceeding 1.02 MeV, the process of pair production becomes energetically possible. The interaction takes place in the coulomb field of the nucleus, where the gamma ray photon disappears and is replaced by an electron-positron pair. The excess energy carried by the photon goes mainly into kinetic energy of the created pair, while little amount of energy ($\mathcal{O}(eV)$) is transferred to the nucleus. The energy transfer to electron and positron in pair production interactions is given by:

$$E_k = h\nu - 2E_e \tag{2.8}$$

After being produced, the positron typically slows down and subsequently annihilates with a nearby electron, resulting in the emission of two annihilation photons. The probability of pair production event is given by the Maximon [7]:

$$\sigma_{pair} = Z^2\alpha\frac{2\pi}{3}r_e^2\Big(\frac{k-2}{k}\Big)^3\Big(1+\frac{1}{2}\rho+\frac{23}{40}\rho^2+\frac{11}{60}\rho^3+\frac{29}{960}\rho^4\Big) \tag{2.9}$$

where $\rho = \frac{2k-4}{2+k+2\sqrt{2k}}$. For energies higher than 2.044 MeV the Maximon equation transforms into:

$$\sigma_{\text{pair}} = Z^2\alpha r_e^2\Bigg\{\frac{28}{9}\ln(2k) - \frac{218}{27} + \left(\frac{2}{k}\right)^2\left[6\ln(2k) - \frac{7}{2} + \frac{2}{3}\ln^3(2k) - \ln^2(2k) - \frac{1}{3}\pi^2\ln(2k) + 2\zeta(3) + \frac{\pi^2}{6}\right] - \left(\frac{2}{k}\right)^4\left[\frac{3}{16}\ln(2k)+\frac{1}{8}\right] - \left(\frac{2}{k}\right)^6\left[\frac{29}{9\cdot 256}\ln(2k) - \frac{77}{27\cdot 512}\right] + f_{corr,pair}\Bigg\} \tag{2.10}$$

where $\zeta(3) \approx 1.2020569$ is the Riemann zeta function.

In equations (2.4), (2.6) and (2.10) there are three correction factor functions ($f_{corr,ph}$, $f_{corr,C}$, $f_{corr,pair}$) [8]. Each of them has different form dependent on the energy. The purpose of those correction factor functions is to obtain a better precision of the cross section in a given energy range.

The total cross section for gamma-ray interactions can be expressed as the sum of the individual contributions listed above:

$$\sigma_{tot} = \sigma_{ph} + \sigma_C + \sigma_{pair} + \sigma_{trip} \tag{2.11}$$

Here σ_{trip} is the cross section of the triplet production interaction mechanism. The triplet production is an interaction, where positron and electron are produced in the field of other electron, with the threshold at 2.044 MeV. This interaction mechanism becomes relevant in an energy range which is not a topic of discussion covered in the present work, therefore details around the cross section formula are omitted. The total cross section for a carbon absorber, together with the contributions from each interaction mechanism, is illustrated in Figure 2.1.

2.2 Detectors for gamma rays

Gamma-ray detectors designs are based on the interaction mechanisms stated above. Those mechanisms result in the production of secondary electrons. As these electrons travel through the detector medium, they loose energy via either ionization or (and) excitation, generating a measurable electrical signal. This signal is then amplified and converted into a voltage pulse, whose amplitude is proportional to the energy deposited by the incident gamma ray. The signal is than transmitted to an analyzing system where it undergoes shaping and digitization. This allows for precise measurement of the signal's properties, which after acquiring numerous events in turn gives information about the energy of the corresponding gamma line, its intensity, and other characteristics. Finally, the digitized data is usually recorded on a separate device where the data is displayed and further analyzed.

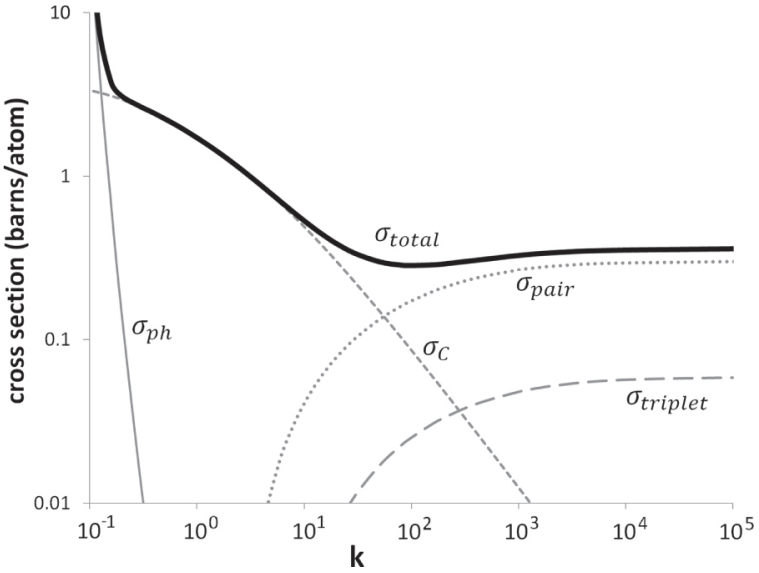

Figure 2.1: The total cross section dependence on k for a carbon absorber as the sum of cross section of the photoelectric effect, Compton scattering, pair and triplet production(from [8]).

2.2.1 Energy measurement

There are different techniques for energy measurement, based on the energy scale in which the impinging gamma quantum falls into. Within each energy scale there are distinct challenges in designing a detector system that is capable of performing a specific task while also being able to achieve high efficiency, resolution, or other important characteristics. Those challenges arise due to the different interaction mechanisms that dominate at different energy scales. Measurement of the deposited energy in the detector system is crucial for accurately reconstructing the source and improving overall imaging and spectroscopy.

2.2.1.1 Low energy scale

At low energies ($\sim$ 0.1 MeV), photons primarily interact through the photoelectric effect, transferring all their energy to electrons in atomic shells. This results in the production of electron-ion pairs in the detector medium, with the number of pairs being directly proportional to the photon's energy. Due to their high interaction cross section, low-energy photons have a short mean free path and are absorbed almost immediately upon entering the medium. Gas-filled detectors such as proportional counters or ionization chambers are well suited in those energy levels, because of their ability to fine-tune the effective thickness of the detection region by adjusting gas pressure, rather than relying on fixed physical dimensions [9],[10]. In particular proportional counters [11] have the advantage of operating on the phenomenon of gas multiplication, which amplifies the charge represented by the original ion pairs created from the passing gamma photon. This is in contrast with the ion chamber, which collects the ions without any multiplication, therefore producing a much smaller signal. Gas multiplication occurs when the electric field within the gas is sufficiently strong to prevent ion pair recombination and to accelerate free electrons to energies high enough

to ionize additional gas atoms and thus produce even more free electrons, which are also accelerated. The resulting chain reaction of ionizations is known as a Townsend avalanche (Figure 2.2), which typically occurs in most gases at atmospheric pressure when the electric field exceeds a threshold of approximately 10^6 V/m [12]. Because of this the total collected charge is multiplied and and the resulting pulse amplitude is larger, than that produced by a primary ionization alone.

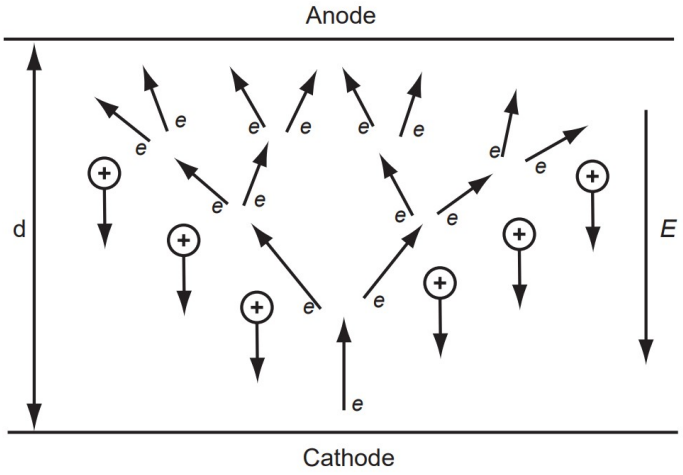

Figure 2.2: Townsend breakdown and electron avalanche formation between two electrodes (from [13]).

Over a specific range of the electric field, the multiplication of the charge becomes linear, meaning the collected charge is directly proportional to the number of primary ion pairs produced by the incident gamma photon. This means that each photon interaction can trigger an avalanche whose size scales with the number of primary electrons. This is what defines the proportionality region – the operating mode of the proportional counter.

A common design for proportional counters is the cylindrical configuration, where a thin wire anode runs along the central axis of a hollow metal tube, which acts as the cathode (Figure 2.3).

Gas multiplication requires a large value of the electric field. In the case of cylindrical geometry, the electric field at radius r is [14]:

$$\mathcal{E}(r) = \frac{V}{r \ln\left(\frac{b}{a}\right)} \tag{2.12}$$

where V is the voltage applied between the anode and the cathode, a is the radius of the anode wire and b is the radius of the cathode wire.

In order to ensure that the signal amplitude depends only on the number of primary ion pairs produced by the incident radiation, a uniform gas multiplication should be achieved. Thus gas multiplication must be confined to a very small region compared with the total gas volume. In this way, nearly all primary ion pairs are created outside the multiplication zone, and each primary electron simply drifts into that region before amplification occurs. As a

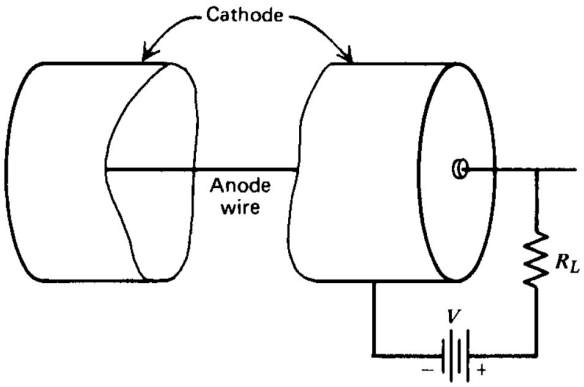

Figure 2.3: Principle scheme of proportional counter. The outer cathode must provide a vacuum-tight enclosure for the fill gas. The output signal is developed across the load resistance R_L (from [14]).

result, every electron experiences the same multiplication process, regardless of where it was initially formed, ensuring that the multiplication factor is identical for all primary ion pairs.

2.2.1.2 Mid energy scale

In the mid-energy range (0.1 - 10 MeV), the process that dominates is Compton scattering. In that case the gamma photon has enough energy to undergo multiple Compton scatterings until it finally gets absorbed in the medium. In this energy range proportional counters become less viable option since the counting efficiency becomes very small, due to the fact that the photoelectric effect section decreases rapidly with the energy of the gamma photon. In such cases, scintillator and semiconductor detectors are preferred due to their high Z number and high density.

Scintillator detectors [15] consist of a scintillating material which is coupled to a photodetector. As a gamma photon passes through the scintillating material, it gets absorbed in the medium. Then the energy is reemited as photons in the visible spectrum through the excitation and subsequent de-excitation of the scintilator's atoms or molecules. This light is then collected and converted into an electrical signal by the photodetector. In general, there are two types of scintilators: organic and inorganic.

Organic scintilators [16] are based on organic molecules, in which scintilating light arises from the transitions made by the free valence electrons of those molecules. The valence electrons are not associated with any particular atom in the molecule and occupy structures known as π-molecular orbitals. Energy can be absorbed by pushing the electrons from their ground state to one of several possible excited states. The ground state called S_0 (Figure 2.4), is a singlet state. Above it there are higher-energy excited singlet states (S^*, S^{**},...), as well as triplet states, with the lowest triplet state denoted as T_0 and its excited levels as T^*, T^{**},.... Each of these so-called electronic states is associated with a fine structure which corresponds to the excited vibrational modes of the molecule. The energy difference between electronic states is a ($\mathcal{O}(eV)$), while the vibrational levels have a difference of about

1/10 of a MeV. When a gamma photon interacts with the organic scintillator, it can excite either an electronic or a vibrational level. Excitations to higher singlet states decay quickly ($\leq 10\ ps$) [17] to the S^* without emitting light. From this state, the molecule decays to one of the vibrational levels of ground state S_0, releasing a photon, which has low enough energy such that a transition of the kind $S_0 \rightarrow S^*$ has no probability to happen and thus the photon can travel in the scintilator without being reabsorbed.

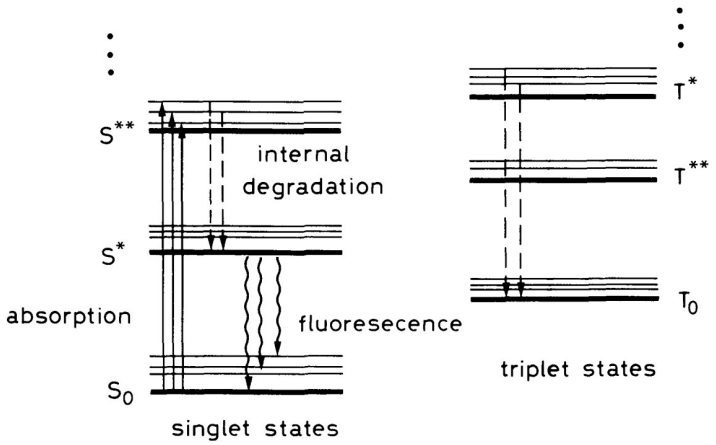

Figure 2.4: Energy level diagram of an organic scintillator molecule. The singlet states (denoted by S) are separated from the triplet states (denoted by T) (image taken from [17]).

Scintillation in inorganic scintillators [18] [19] operates through a different mechanism compared to organic materials. As opposed to the scintillation mechanism in organic materials, that in inorganic scintillators is governed by the electronic band structure of the crystal. Electrons have available only discrete bands of energy (Figure 2.5).The band structure consist of a lower band, called the valence band, which represents the electrons that are bound at the crystal's lattice sites, whereas the conduction band represents those electrons that have sufficient energy to be free to migrate throughout the crystal medium. There exists an intermediate band of energies, called the forbidden band, in which electrons can never be found in a pure crystal. Absorbing a photon leads to elevation of an electron from the valence band across the forbidden gap into the conduction band, leaving a hole in the valence band. Eventually, the electron goes back to the valence band via an emission of a photon. To increase the probability for photon emission and to reduce self-absorption, small amounts of impurities called activators are added to the crystal [21]. That is why inorganic scintillators are typically composed of alkali halide crystals doped with a small concentration of activator impurities. An example of this is NaI(Tl), where Thallium (Tl) is the impurity activator.

Scintilator crystals have many important properties, the most important being light yield and decay time. Light yield is the number of photons in the visible spectrum produced per unit of energy deposited. This number is directly related to the energy resolution of the detector. The other property called decay time refers to the characteristic time over which the scintillation light output decreases exponentially after excitation. The decay time of the induced scintilation should be short so that fast signal pulses can be generated. Other

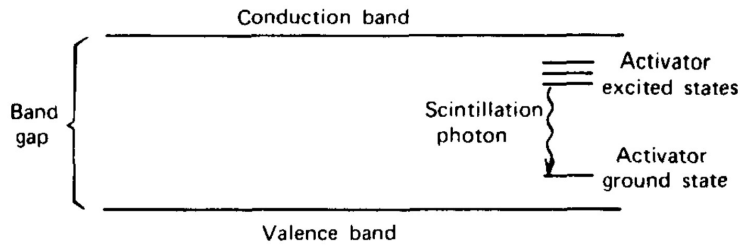

Figure 2.5: Energy band structure of an activated crystalline scintillator ([20]).

important properties are index of refraction, higroscopicity, etc.

Scintilators are usually coupled to photodetectors [22], which convert the scintillation light into an electrical signal. A common type of photodetector is the photomultiplier tube (PMT). PMT-s are typically constructed with an evacuated glass housing, containing a photocathode, several dynodes, and an anode (Figure 2.6). Upon registering a photon, the photocathode releases a number of electrons, which are then multiplied and focused by the dynodes.

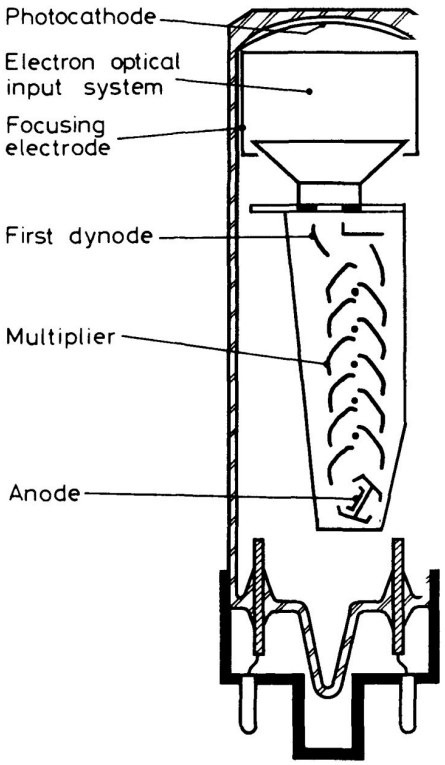

Figure 2.6: Schematic diagram of a photomultiplier tube (from [23]).

After the number of electrons is multiplied through the dynode structure, a typical

scintillation pulse will give rise to $10^7 - 10^{10}$ electrons [24], which is sufficient to serve as an output charge signal from the original scintillation event. The total charge produced by the dynode structure is then collected at the anode.

An alternative to PMTs are silicon photomultipliers (SiPMs). A SiPM [25] consists of an array of microcells, where each microcell is made up of an avalanche photodiode operated in Geiger mode and connected in series with a quenching resistor. All microcells are connected in parallel, so the SiPM has two external terminals: an anode and a cathode. The device is externally biased such that each photodiode operates at a voltage slightly above its breakdown voltage. This excess bias is referred to as the overvoltage, and SiPM performance parameters - such as gain and photon detection efficiency, are proportional to it, thus making it an important quantity of the SiPM. When a photon is absorbed in a microcell, it generates an electron–hole pair. The high electric field in the junction of the photodiode structure separates the pair and accelerates the the electrons. This acceleration initiates an avalanche, resulting in the multiplication of the initial charge and producing approximately $10^5 - 10^6$ electrons. To stop the avalanche, each microcell includes a quenching resistor, which limits the current and reduces the voltage across the junction, thereby quenching the avalanche and allowing the microcell to reset and go back to Geiger mode.

An alternative to scintillator detectors are semiconductor detectors [26]. Their advantage lies in the smaller forbidden region in their band structure, which enables superior energy resolution compared to scintillator detectors.

A key feature in semiconductor detectors is the size and formation of a p–n junction. This junction is formed by bringing together two regions of a semiconductor material with different doping types, p-type, which is rich in holes, and n-type, which is rich in electrons. At the surface interface between these two regions, charge carriers diffuse across the junction and recombine, creating a region depleted of free charge carriers known as a depletion region Figure (2.7).

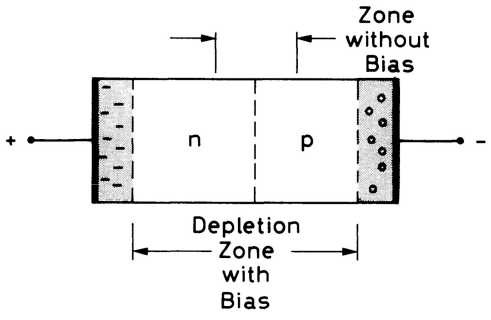

Figure 2.7: Reversed-bias junction ([27]).

This region acts as the active volume of the detector. When a reverse bias voltage [28] is applied across the p–n junction, the depletion region widens significantly. Upon an interaction with a gamma photon and absorbtion of its energy, numerous electron-hole pairs are created in the forbidden region. Under the influence of the electric field inside this region the electrons and the holes are accelerated toward the electrodes, thereby producing a current signal, which holds information about the energy of the incident gamma photon. Even

without the gamma photon interaction, electron-hole pairs are constantly being generated by thermal energy. After their formation, they take part in a random thermal motion that results in the diffusion away from their point of origin.

Commonly used materials for semiconductor detectors are silicon and high-purity germanium (HPGe). For detection of gamma rays, germanium is a superior material, because of its much higher atomic number ($Z_{Si} = 14$, $Z_{Ge} = 32$). The photoelectric cross section is thus about 60 times greater in Ge than Si [29]. A key feature of high-purity germanium detectors is the thickness d of their depletion region, which is determined by [30]:

$$d = \left(\frac{2\varepsilon V}{eN}\right)^{1/2}, \tag{2.13}$$

where ϵ is the dielectric constant, V is the reverse bias voltage, and N is the number of impurities. This reversely proportional relation between the thickness and the number of impurities is what constitutes the need for achieving high amounts of purity in germanium detectors. One disadvantage of germanium detectors is that they need to be cooled off continuously during operation in order to suppress the current arising from thermal excitation.

2.2.1.3 High energy scale

For gamma photons with energies exceeding 10 MeV, pair production becomes the dominant interaction mechanism. In this energy range, electromagnetic calorimeters are essential for accurately measuring the deposited energy. In that case when a high energy photon interacts with matter, it is converted into electron and positron pair, which then emit energetic bremsstrahlung photons. This results in a cascade of photons, electrons and positrons (Figure 2.8).

This process continues until the energy of the pair produced electrons and positrons is below some critical energy E_c. The maximum number of particles produced in a single shower event is [31]:

$$N_{\max} \simeq \frac{E_0}{E_c}, \tag{2.14}$$

where E_0 is the energy of the incident gamma photon.

The materials used in calorimeters as well as their mass and size is determined by the energy loss characteristics of the showers. The energy loss is characterized by the formula:

$$\frac{dE}{dt} = E_0 b \frac{(bt)^{a-1} e^{-bt}}{\Gamma(a)}, \tag{2.15}$$

where a and b are parameters dependent on the material of the calorimeter, and $t = \frac{x}{X_0}$, where X_0 is the radiation length. If this equation is solved for t, it gives the maximum penetration depth of the shower :

$$t = (a-1)/b = 1.0 \times (ln\ y + C_i)\ , i = e, \gamma, \tag{2.16}$$

where $y = \frac{E_0}{E_C}$ and $C_e = -0.5$ for electrons and $C_\gamma = 0.5$ for photons.

In general, there are two types of calorimeters - sampling and homogeneous. In homogeneous calorimeters, a single material constitutes the entire active volume, serving both as

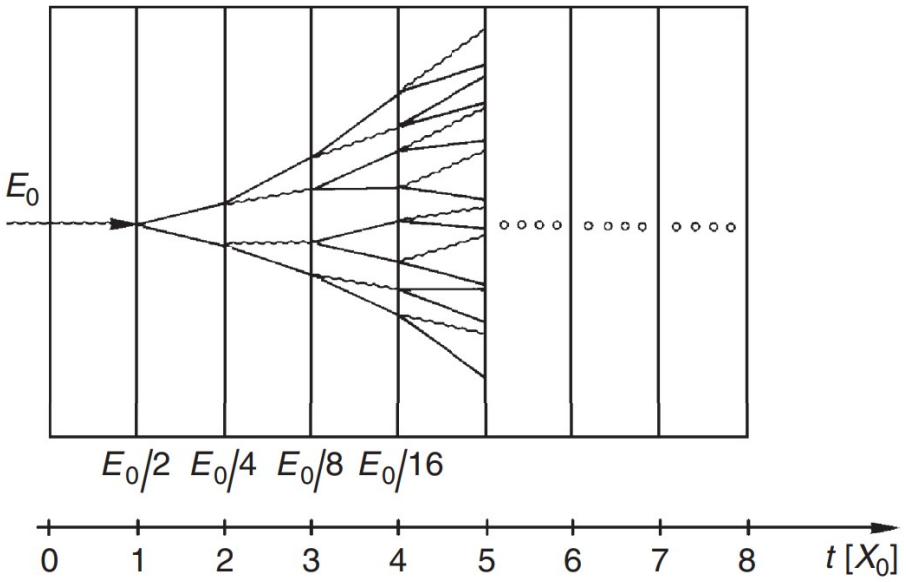

Figure 2.8: Sketch of electromagnetic shower. The horizontal axis shows how the average energy of each member of the pair scales with t (from [32]).

the absorber, where particle showers are produced, and as the detector medium, which generates the measurable signal. Main advantage of those type of calorimeters is their excellent energy resolution, which is due to the fact that the whole energy of an incident particle is deposited in the active volume. However, homogeneous calorimeters are less easily segmented laterally and longitudinally, which is a drawback when position measurements and particle identification at high energies are needed. Sampling calorimeters on the other hand consist of alternating layers of absorber and active medium. This results in a generally worse energy resolution, but consecutively it also means that their readout can easily be segmented longitudinally and laterally, and therefore they usually offer better spacial resolution and particle identification. Sampling calorimeters are mainly used for measurements of hadronic showers, since they provide enough interaction lengths with a reasonable detector thickness, while for high energy resolution measurement of gamma photons, homogeneous calorimeters are the preferred choice [33].

2.2.2 Direction measurement

Besides energy measurement, one may also want to measure the direction of the impinging gamma photon in order to gain insight about where it comes from and consequently identify the spatial coordinates of the source, from which it originates.

2.2.2.1 Tracking of the recoil electron

In the sub-MeV energy range, the direction of the incident photon can be estimated by using recoil directions of electron tracks produced during Compton scattering. Since the

photon transfers a portion of its energy and momentum to the electron, the trajectory of the recoil electron carries information about the photon's original direction. Thus tracking of the recoil electron will help constrain the Compton circle to a point and a significant background reduction can be achieved, compared with the conventional Compton cameras, where the incident direction of a gamma ray is estimated by a cone (Figure 2.9). The integration of electron tracking significantly mitigates the occurrence of these artifacts. For an electron-tracking Compton camera, the unit vector representing incident direction of the incident gamma ray can be calculated using the formula [34]:

$$\vec{s}_{\text{res}} = \frac{E_2}{E_1 + E_2}\,\vec{g} + \frac{\sqrt{E_1(E_1 + 2m_e c^2)}}{E_1 + E_2}\,\vec{e} \tag{2.17}$$

where $\vec{g}$, and $\vec{e}$ denote the unit vector of the scattered gamma-ray, and unit vector of the recoiled electron, respectively. The quantities E_1 and E_2 correspond to the kinematic energy of the recoiled electron E_e and the energy of the scattered gamma photon E'_γ, if the event includes only one Compton scattering event and one photoabsorption event.

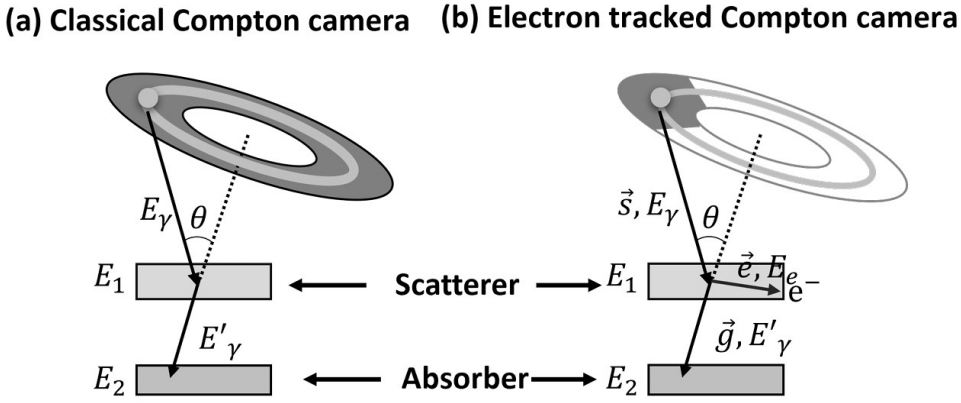

Figure 2.9: Principle of a conventional Compton camera (left) and an electron-tracking Compton camera (right) (from [34]).

2.2.2.2 TPC tracking

Another method of measuring the trajectory of the gamma photon passing through matter is through the usage of time projection chamber (TPC). A TPC [35] is a three-dimensional tracking detector capable of providing information on many points of a particle track along with information on the specific energy loss, $\frac{dE}{dx}$, of the charged particle. The TPC could be divided into two halves, as shown in (Figure 2.10), by means of a central electrode. When voltage is applied, a uniform electric field directed along the direction of the readout plates in the end of the cylinder is created. Gas, usually a mixture of argon and methane, is introduced in the chamber. Upon interaction of the gamma photon with the mixture of gases, a primary ionization occurs, resulting in the ejection of one or more electrons. The electrons drift towards the readout plane which consists of anode wires parallel to which are

cathode strips cut up into rectangular segments. This provides the location of a space point as projected onto the readout plate. One coordinate is given by the position of the firing anode wire while the second is obtained from the signals induced on the row of cathode strips along the anode wire [36].

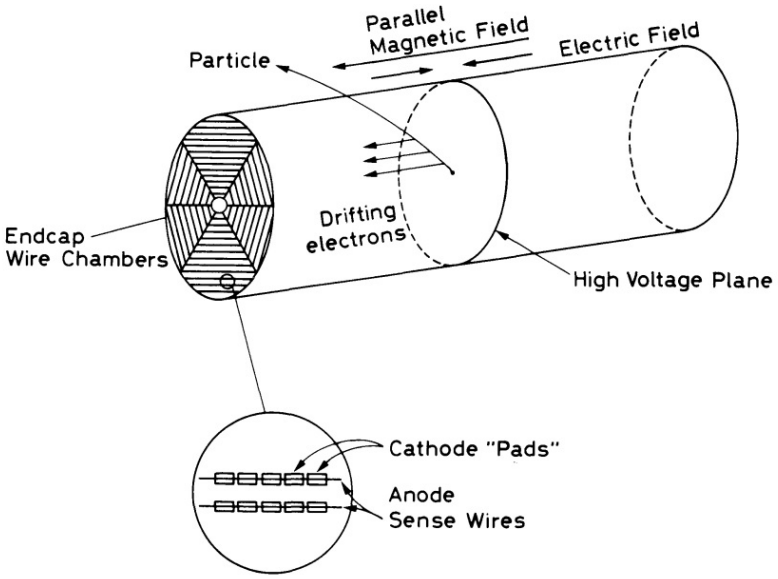

Figure 2.10: Schematic diagram of a time projection chamber(from [36]).

Using the center of gravity method, the position of the avalanche along the firing anode wire can be located. The center of gravity method exploits the signals induced on the cathode strip. The induced signals have the biggest value on the strip closest to the avalanche point. This value diminishes proportionately with distance from the avalanche point. If y_i is the coordinate of the i-th strip and Q_i is the measured charge on that strip, then the avalanche point can be estimated by calculating the center of gravity [37]:

$$y = \frac{\sum(Q_i - b)y_i}{\sum(Q_i - b)} \tag{2.18}$$

where b is a small bias which is subtracted from each Q_i in order to correct for the dispersive effects of noise. The z coordinate is determined by measuring the drift time from the ionization event to the readout panel, while the x and y direction are determined by the position of the electron clusters detected on the readout plate. Parallel to the electric field there is also a magnetic field applied along the length of the chamber, in order to minimize the diffusion of the electrons coming from the ionization of the gas. During operation, a potential issue is the accumulation of space charge within the drift volume, caused by positive ions generated in avalanches that drift back towards the central cathode. The number of these ions can become large enough to cause distortions in the electric field within the drift volume. To mitigate this effect, a grid held at ground potential is installed. Those grids are placed just

before the anode wires, so that positive ions get captured at this grid rather than drifting back into the active volume of the detector. The grid additionally isolates the drift region from the avalanche region, enabling independent control of both areas.

2.2.2.3 Tracking of an electron-positron pair

As discussed in previous sections, high-energy gamma photons interact with matter primarily via the pair production mechanism. The resulting electron–positron pair, produced at the site of the original gamma-ray interaction, is subsequently tracked through high-resolution tracking detectors to reconstruct the photon's trajectory. After that the pair deposits its energy in electromagnetic calorimeter, thus measurements of the direction and the energy of the gamma ray are obtained. An example of this principle is the detector used in the FERMI - LAT experiment (Figure 2.11).

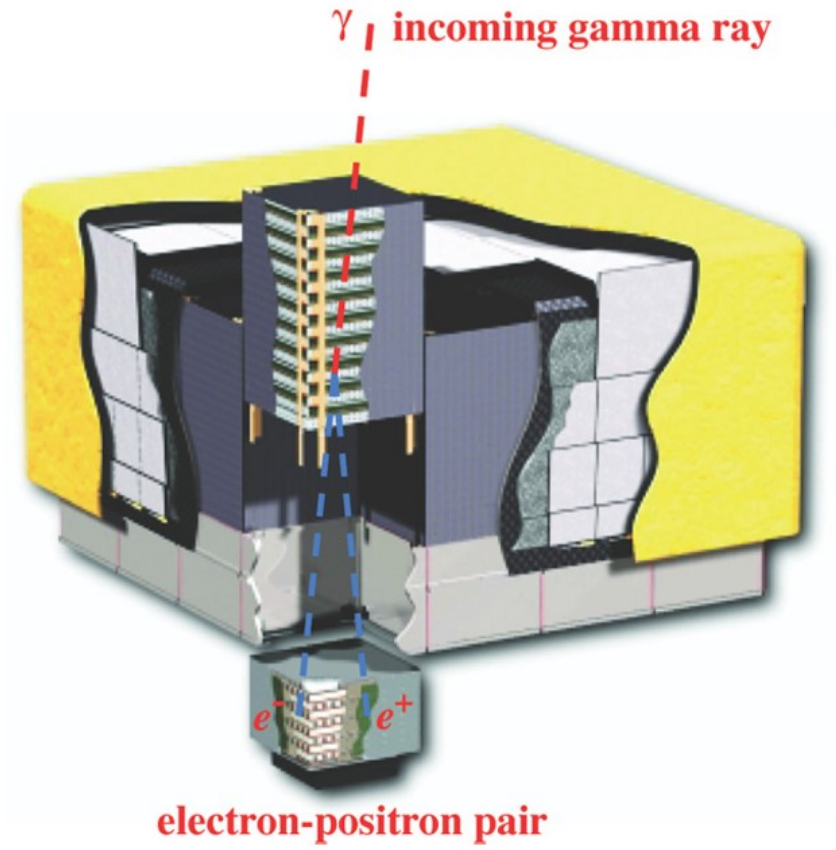

Figure 2.11: Schematic diagram of the LAT (from [38]).

The LAT [38] is a pair-conversion telescope composed of a precision converter–tracker and a calorimeter, each made up of a 4×4 array of modules within a lightweight aluminum grid. A segmented anticoincidence detector covers the tracker, and a programmable trigger/DAQ system combines signals from all three subsystems to generate event triggers.

The converter-tracker has 16 planes of high-Z material on which incident gamma rays are converted to electron-positron pairs. The converter trackers are intermixed with position-sensitive detectors to track charged particles from pair conversion and reconstruct the direction of the incident gamma ray. Each tracker module contains 18 tracking planes, each with two layers of single-sided silicon strip detectors (x and y). The tracker serves as the primary trigger for the LAT, generating a first-level trigger when signals from successive detector layers coincide.

After the tracker determines the trajectory of the electron–positron pair, the particles enter the calorimeter, where they deposit their energy through the initiation of electromagnetic shower. Each calorimeter module is built from 96 CsI(Tl) crystals, which are optically isolated to prevent light sharing between neighboring elements. The crystals are arranged into eight horizontal layers of 12 crystals each, with successive layers rotated by 90 ° to create a (x, y) hodoscopic configuration.

The final subsystem in the LAT telescope is the anticoincidence system (ACD). The purpose of the ACD is to provide charged-particle background rejection;therefore its main requirement is to have high detection efficiency for charged particles. The ACD consists of 89 plastic scintillator tiles, overlapped, with scintillating fibers covering seams. The signals of charged particles are then measured by photomultiplier tubes. A characteristic gamma ray event in the LAT is therefore represented by no signal in the ACD, more than one track starting from the same location within the volume of the tracker, and an electromagnetic shower in the calorimeter.

Chapter 3

Compton camera

3.1 Basic principle of operation

A Compton camera is a gamma-ray detection system that utilizes the kinematic principles of Compton scattering to reconstruct the incoming photon's trajectory [39]. By measuring the energy and interaction positions of scattered gamma rays within the detectors it is possible to infer the direction of the incident photon.

A basic Compton camera consists of two subdetectors: a scatterer and an absorber. A gamma photon scatters in the scatterer at an angle θ_C, depositing an amount of energy E_1, after which it is captured in the absorber, depositing its remaining energy E_2. Through the energy deposited at each of the two interaction points in the detectors and through the implementation of the Compton kinematics described in section 2.1 the scattering angle θ_C can be calculated. The scattering angle and the interaction positions constrain the origin of the incident photon to a cone surface, and the position of the gamma source can be located by finding the intersection of the cones that correspond to many different measurements. The region with the highest cone density (i.e. most intersections) indicates the most probable source direction. The type of Compton cameras that use this type of location estimation are called back-projection Compton cameras. Generally this type of Compton camera produces false spots in the reconstructed image, because the back-projection method estimates the probability distribution of the location of a radiation source as a circle. As discussed in section 2.2.2.1 tracking of the recoil electron would reduce the Compton circle to a point (spot) and a significant background reduction can be achieved. Alternatively, the quality of the reconstructed image can be improved by employing reconstruction methods other than simple back-projection.

In the method described by Daniel et al. [40], the intersection of each Compton cone with a plane z occurs at coordinates (x, y) where the function S is zero and will be either full or partial ellipse:

$$S = \left|(\cos\theta)^2 \left[(x-x_1)^2 + (y-y_1)^2 + (z-z_1)^2\right] - \left[n_x(x-x_1) + n_y(y-y_1) + n_z(z-z_1)\right]^2\right|. \tag{3.1}$$

Because the 3D image space is divided into voxels (the smallest unit in a 3D object), the exact cone surface rarely aligns with voxel centers. A distance map $S(x, y, z)$ is computed, indicating how close each voxel is to the true elliptical intersection. A threshold function

is then applied to convert this continuous distance map into a binary representation of the elliptical intersection. This means that voxels with values below a chosen threshold are classified as part of the intersection and assigned a value of one, while all others are excluded by setting their value to zero. The threshold is not fixed, but varies depending on both the height of the plane (z) and the cone angle (θ), due to geometric changes in how the cone intersects each plane. This adaptive thresholding approach allows for more accurate reconstruction by selecting only those voxels that lie close to the true cone surface.

Another method utilizes the List-mode Maximum Likelihood estimation to determine the most probable source distribution that could have produced the observed Compton scattering data [41]. List-mode reconstruction is preferred in Compton camera image reconstruction, because the total number of elements in the data list, which is the set of detected photon events, is typically much smaller than the total number of possible position and energy combinations. This results in a significantly reduced computational problem compared to more traditional iterative methods. A general equation for this method is:

$$\lambda_j^n = \frac{\lambda_j^{n-1}}{S_j} \sum_{i=1}^{N} \frac{t_{ij}}{\sum_k t_{ik} \lambda_k^{n-1}}, \tag{3.2}$$

where λ_j^n represents the calculated amplitude of the image pixel j at the n-th iteration, N is the number of recorded events, and t_{ij} is the weighted likelihood when event i originated from image pixel j. The sensitivity S_j denotes the probability that a gamma ray originating from image pixel j is detected anywhere in the camera.

Yet another method for image reconstruction is the stochastic origin ensemble (SOE) method, which was introduced by Andreyev et al (2009)[42]. The imaging algorithm is based on the Monte Carlo Markov chain algorithm, which assumes that each event is associated with a pixel of the reconstructed image. With respect to the transition probability, each event may move to another pixel for each iteration. For the initialization of this iterative method, the possible origin points and their new location within a back-projected cone are randomly selected. Finally, the pixel values of the former and new candidate points are compared in accordance with the acceptance probability; the former point or the current point will be the new point. The image is than reconstructed using the estimated new location for all the events. The probability for an event to transition to a new location is given by:

$$p_i = \min \left(1, \frac{(d(n_i)+1)^{d(n_i)+1} \, (d(o_i)-1)^{d(o_i)-1}}{d(n_i)^{d(n_i)} d(o_i)^{d(o_i)}} \right) \tag{3.3}$$

where for the i-th former event, n_i is the new selected position, o_i is being the old position, and the transition probability is given by p_i.

3.1.1 Classification of Compton Camera Designs

In addition to the diverse techniques developed for image reconstruction, a wide range of Compton camera configurations has also been proposed and implemented, each tailored to a specific application requirements and performance goals. In previous sections electron-tracking Compton cameras were discussed, but they represent only a specific case within the broader class of Compton camera imaging systems.

3.1.1.1 Semiconductor-based Compton Cameras

A widely studied and implemented variant of the Compton camera is the semiconductor-based design, which offers high energy resolution and precise position determination. Among the variety of semiconductor materials Si and CdTe are considered suitable for gamma ray measurements. The Compton cross-section for Si becomes relatively large, due to its small atomic number($Z = 14$). Additionally, Si has a smaller Doppler broadening effect compared to other materials with higher Z. These characteristics make Si an effective choice for use as a scattering medium. On the other hand, CdTe makes for a good absorber, due to its high photo-absorption efficiency for gamma-rays in this energy region because of the high atomic numbers of Cd and Te ($Z_{\mathrm{Cd}} = 48$ and $Z_{\mathrm{Te}} = 52$). An example of the potential effectiveness of a Si/CdTe based Compton camera is presented in Shin Watanabe et al (2007) [43]. The basic concept of such camera is illustrated in Figure 3.1. Si and CdTe imaging detectors were developed for the Compton camera. A four layer Double-sided Si strip detectors (DSSD) stack and a four layer CdTe pixel detector stack were, respectively, constructed as a scatterer detector and an absorber detector for the Compton camera. With the DSSD stack, an energy resolution of 1.5 keV (FWHM) was obtained for 60 keV gamma-ray photons, while for the CdTe pixel detector stack, a $\Delta E/E \sim 1\%$ energy resolution (FWHM) was achieved.

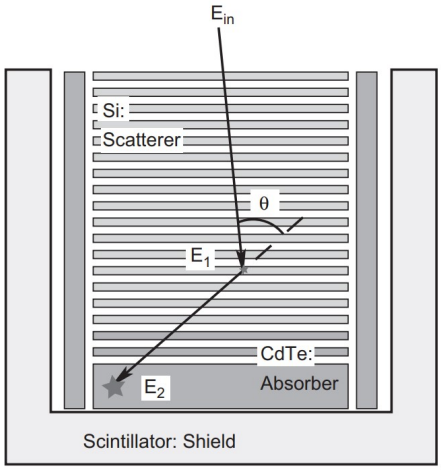

Figure 3.1: Schematic picture of the proposed Si/CdTe semiconductor Compton camera (from [43]).

Another widely used type of semiconductors for the construction of Compton cameras are Ge semiconductors. *Ge* offer several advantages over other conventional semiconductors. For instance, *HpGe* has an excellent energy resolution of approximately 0.2% at $662keV$ [44], which surpasses the performance of *Si* based detectors. This superior energy resolution enables more precise gamma-ray spectroscopy, allowing better identification of gamma-ray lines. *Ge* has a conveniently high Compton scattering cross-section for a large range of gamma ray energies [46] which makes it a suitable choice for both scatterer and absorber medium when constructing a telescope. Similar to Si, *Ge* possesses a relatively low Doppler

broadening of the scattered gamma-rays [45]. One major drawback of HpGe based detectors is that they need a sufficient amount of cryogenic cooling in order to reduce thermal noise. Despite this, the enhanced resolution and efficiency make $HpGe$ detectors a preferred choice when constructing Compton telescope systems. An example of such system is presented in Alnaaimi et al (2011) [47], where the camera consists of two pixelated germanium detectors in a nitrogen cooled vacuum housing made of aluminum Figure 3.2.

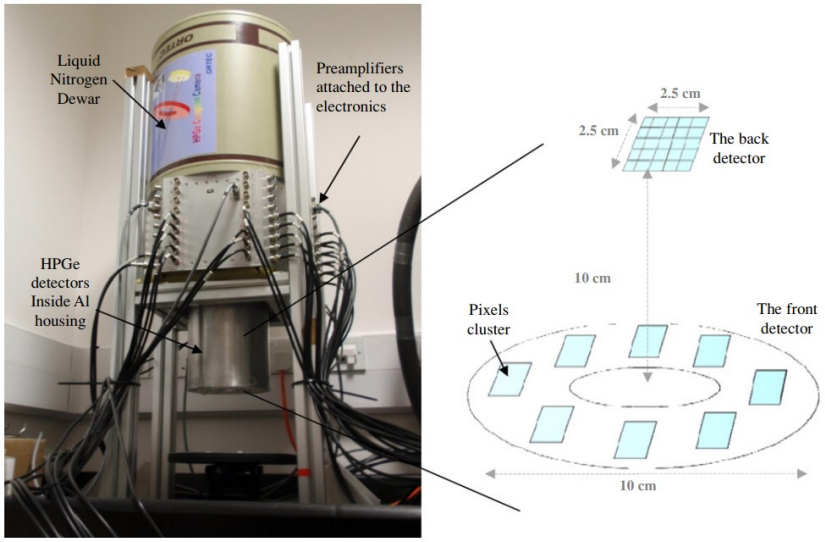

Figure 3.2: A photograph of the HPGe Compton camera (left) with the configuration of the front and back detectors(right) (from [47]).

The camera has a total of 177 pixels, with 152 in the scatter detector and 25 in the absorption detector. The pixels measure 4×4 mm^2, with a thickness of 4 mm in the scatter detector and 10 mm in the absorption detector. Images were acquired from variety of test objects, such as point sources, a ring source, and a Perspex phantom. The measured angular resolution is $9.4^\circ \pm 0.4^\circ$ for a 662 keV gamma ray source at a distance of 3 cm.

3.1.1.2 Scintilator-based Compton Cameras

Unlike semiconductor detectors, scintillator-based Compton cameras can operate at room temperature. They offer high detection efficiency and are generally more cost-effective. However, their energy and spatial resolution are inferior compared to semiconductor detectors. The variety of scintillator materials commonly employed in Compton cameras due to their favorable detection characteristics are $NaI(Tl)$, $CsI(Tl)$, $Ce:GAGG$, and more. Each of those materials offers distinct advantages, making them suitable for different applications depending on the specific requirements of the system. For example $NaI(Tl)$ and $CsI(Tl)$ scintillators offer high sensitivity, but have poor energy resolution in the low-energy range. This limitation is particularly relevant for medical imaging, where most radiopharmaceuticals emit gamma rays with energies below 250 keV. However, despite this $NaI(Tl)$ and $CsI(Tl)$ remain valuable for environmental monitoring [48],[49].

On the other hand, Ce:GAGG scintillators exhibit superior performance compared to other scintillators owing to their emission peak at 520 nm , which arises from Ce^{3+} $5d \rightarrow 4f$ transitions. This makes them well suited for the commercially available photomultiplier tubes PMTs and silicon photodiodes (SiPD) which are sensitive exactly in the same wavelength range[50],[51]. The crystal also possesses a high light yield, a fast light decay time constant with low self-radiation, and a good energy resolution. In certain applications, Ce:GAGG scintillators are even preferred over semiconductors, such as Si/CdTe, because the latter exhibits a lower sensitivity for gamma rays from ^{137}Cs (662 keV) and ^{134}Cs (604 keV) measurements. Another advantage of a Compton camera utilizing Ce:GAGG scintillators is its compact design and the fact that it does not require any cryogenic cooling systems. Such is the proposed camera in J. Kataoka et. al [52], where 50×50 array of $1 \times 1 \times 10$ mm^3 Ce:GAGG scintillator elements for both the scatterer and the absorber were adopted, along 8×8 MPPC array boards which measure the scintillating light using a resistive charge division network. A prototype of the proposed module is shown on Figure 3.3 The energy resolution obtained with the prototype is 9.8% (FWHM).

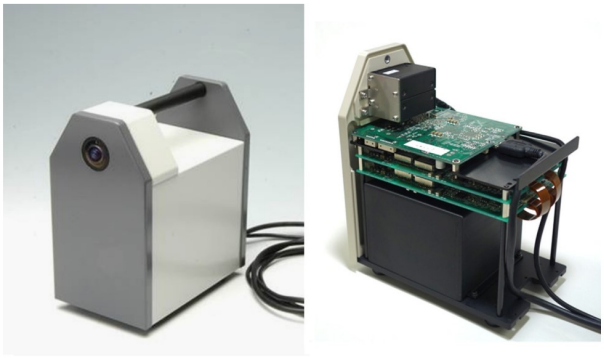

Figure 3.3: Photographs of the Compton camera prototype. Left photograph shows the complete compact form, while the right one shows the internal circuitry of the camera ([52]).

3.2 Applications of directional gamma ray measurements

3.2.1 Medical applications

Compton cameras have significant role in nuclear medical imaging. The main molecular imaging modalities in nuclear medicine are PET and SPECT and they play a crucial role in assessing physiological functions and biochemical alterations in molecular targets. PET imaging relies on the detection of gamma rays emitted by a positron-emitting radioactive tracer that is administered into the body. When the emitted positron encounters an electron, the two annihilate, producing a pair of 511 keV gamma photons that travel in nearly opposite directions. The annihilation photons are detected by PET systems, which commonly use scintillators coupled with photodetectors, enabling image reconstruction. On the other hand, SPECT imaging is based on the detection of gamma rays from radioisotopes tracers such as Tc and I. In the PET method the two annihilation photons provide an opportunity for

coincidence measurements, which leads to more radiation event localization data and, thus, higher spatial resolution images than SPECT.

Both methods mostly rely on the usage of conventional gamma camera. Conventional gamma cameras rely on mechanical collimators to determine the direction of incoming gamma rays by only allowing those traveling along specific paths to reach the detector [53]. However, this approach imposes an inverse relationship between spatial resolution and detection sensitivity. Achieving higher spatial resolution requires narrower collimator holes, which results in a fewer incoming photons being detected. But as a result, the number of detected gamma rays decreases, leading to lower detection efficiency. Compton cameras address the limitations in conventional gamma cameras by employing electronic collimation based on Compton scattering kinematics. This method allows Compton cameras to achieve high spatial resolution while maintaining significantly higher photon detection efficiency compared to mechanically collimated systems. The proposed setup is simultaneous PET–Compton detector [54] (Figure 3.4), which was constructed for proof-of-concept simultaneous PET and SPECT imaging. It consists of an 8×8 multipixel photon counter (SiPM/MPPC) array, with each pixel individually coupled to a $2.5 \times 2.5 \times 9\ mm^3$ Ce:GAGG scintillator.

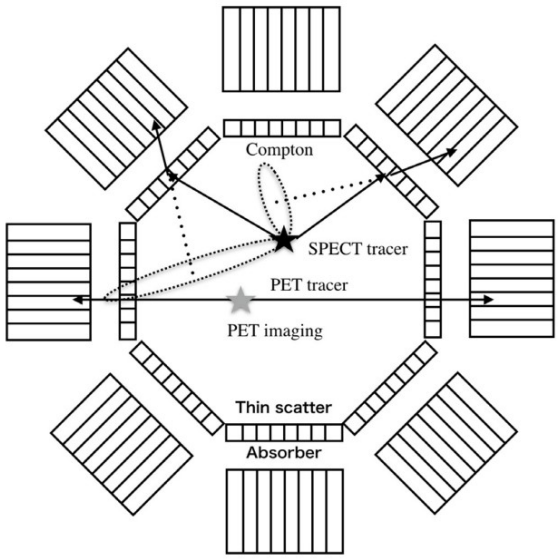

Figure 3.4: . Conceptual schematic of PET–Compton hybrid imager consisting of thin and thick energy-resolving detectors (from [54]).

In comparison with its application in nuclear medical imaging, there is also research on the feasibility of the application of Compton cameras in particle radiotherapy, especially in proton therapy. In proton therapy, there is uncertainty in the exact position of the distal fall-off of the proton Bragg peak. This uncertainty in the range of the proton beam delivered during treatment can lead to under- or over-penetration of the beam, resulting in a geometrical miss of the tumor or delivery of excessive dose to adjacent healthy tissues and critical organs. As a means of overcoming the limitations in proton radioterapy caused by range uncertainties Jerimy C Polf et all (2015) [55] present a prototype of a Compton

camera, which was able to measure prompt gamma emission during delivery of both 114 MeV and 150 MeV proton beams in a water phantom at clinical beam currents. The setup described in the paper was able to produce prompt gamma ray images and also detect the shift in the range of the Bragg peak, thus proving that in vivo range verification during proton treatment delivery using a Compton camera is a feasible concept.

3.2.2 Space applications

In gamma ray astronomy, the detection of gamma photons in the ranges of up to 1 MeV and 1-10 MeV, is challenging due to low photon signals, contaminated backgrounds, and the complex Compton scattering process that occurs in detectors.

In the field of astrophysics, determining the position of a gamma-ray source and measuring its emitted energy are essential for probing cosmic phenomena like gamma-ray bursts, supernova remnants, gamma-ray pulsars, etc. A well known example of the applications of Compton cameras for space studies is the COMPTEL instrument [56], which conducted the first complete all-sky survey in the energy range of 0.75 to 30 MeV, and the highest survey sensitivity was obtained in the energy range of 1–10 MeV. COMPTEL, which was on board of the CGRO (Compton Gamma Ray Observatory), consists of two detector assemblies, an upper one of liquid scinitillator NE213, and a lower one of NaI (Tl). Each of the detectors is monitored by a number of PMT-s. Time of flight measurements are made in order to discriminate forward moving gamma rays from backward moving gamma rays, so that significant background reduction can be achieved. Each detector assembly is surrounded by two anti coincidence shields, so that charged particles can be rejected. The telescope has wide field of view of around 1 steradian, within which distinct sources can be resolved provided they are separated by about 3–5° (depending on energy). The resulting source localization accuracy is of the order of 1°, while the energy resolution achieved is from 5–10% FWHM.

There is a potential for even deeper sky-survey in the MeV range, through the usage of electron tracking Compton camera as proposed in Takada et al (2022) [57]. As discussed in previous sections, electron tracking greatly reduces background noise and enhances detection sensitivity. The electron tracking Compton camera proposed in Takada et al (2022) consists of a scatterer made of a gaseous electron tracker, while pixelated scintillator arrays serve as the absorber. The electron tracking Compton camera was attached to a balloon during the SMILE-2+ mission, where it successfully detected gamma rays from the Crab Nebula with 4.0 σ significance in the 0.15–2.1 MeV range for a period of 5.1 hours. The estimated sensitivity of the electron tracking Compton camera proved to be better than that of COMPTEL, thus promising a significant advance for gamma ray astronomy in the MeV range.

Another project aiming to surpass COMPTEL's results is e-ASTROGAM [58], which utilizes the principle of the Compton camera and pair production, thus extending the energy range in which measurements can be made. The e-ASTROGAM telescope was proposed to be made up of three detection systems: trackers made of 56 planes of double-sided Si strip detectors in which the cosmic gamma-rays undergo a Compton scattering or a pair conversion; a calorimeter made of an array of CsI(Tl) bars and used to absorb and measure the energy of the secondary particles and an anti coincidence system composed of a plastic scintilator to veto the prompt-reaction background induced by charged particles. The performance of the above proposed system is evaluated through simulations using advanced

numerical tools, the results of which show that e-ASTROGRAM will achieve:

- Broad energy coverage from 0.15 MeV to 3 GeV, offering up to two orders of magnitude improvement in the 0.3–100 MeV range compared with earlier missions.
- Unprecedented angular resolution across the MeV range and above several hundred MeV, improving on the angular resolution of the COMPTEL telescope (CGRO) and Fermi-LAT by a factor of ∼4 at 5 MeV and 1 GeV. respectively
- Excellent sensitivity to key gamma-ray lines (for example the 847 keV line due to the decay of ^{56}Co from Type Ia SNe)
- Large FOV (>2.5 sr), which makes the instrument ideal for detecting transient Galactic and extragalactic sources, such as Gamma ray burst (GRB).
- Timing accuracy of 1μs (at 3σ), enabling detailed studies of magnetars, rotation-powered pulsars, and terrestrial gamma-ray flashes (TGFs).

The improved angular resolution would enable a better source identification and localization accuracy as shown in Figure 3.5.

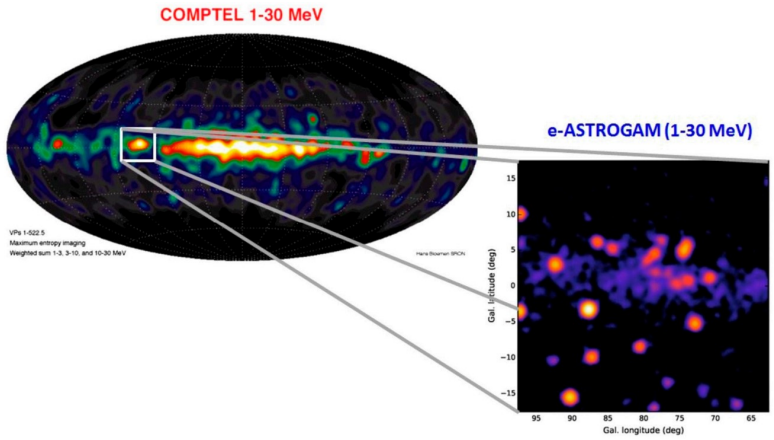

Figure 3.5: 1–30 MeV gamma-ray sky as observed by COMPTEL in the 1990s (upper left) and the simulated Cygnus region in the 1–30 MeV energy range expected from e-ASTROGAM (lower right) (from [58]).

3.2.3 Environment monitoring

It is a necessary practice for nuclear power plants to ensure minimum amount of radiation leakage in the environment and to ensure radiation exposure to workers remains in the established safe limits via constant monitoring. Achieving this requires the ability to accurately localize radiation sources from distances exceeding several meters and across wide areas. Three types of gamma ray detectors are commonly used to localize gamma ray

emitting radioactive sources: pinhole cameras [59], coded-aperture gamma ray cameras [60], and Compton cameras [61]. The detection efficiency of a pinhole camera is limited by the small geometrical area of its aperture, while coded-aperture cameras require higher detection efficiency to be effective in low-level contamination areas (below 1 Sv/h). Therefore Compton cameras present themselves as a strong candidate for environmental radiation monitoring. In Sato et al. [62] a radiation imaging system consisting of a Compton camera and a multicopter drone (Figure 3.6) was developed in order to remotely measure the radiation contamination inside the Fukushima Daiichi Nuclear Power Station. The usage of remotely operated systems is crucial, due to the advantage that the drone can move about in several radiation fields, without much obstruction.

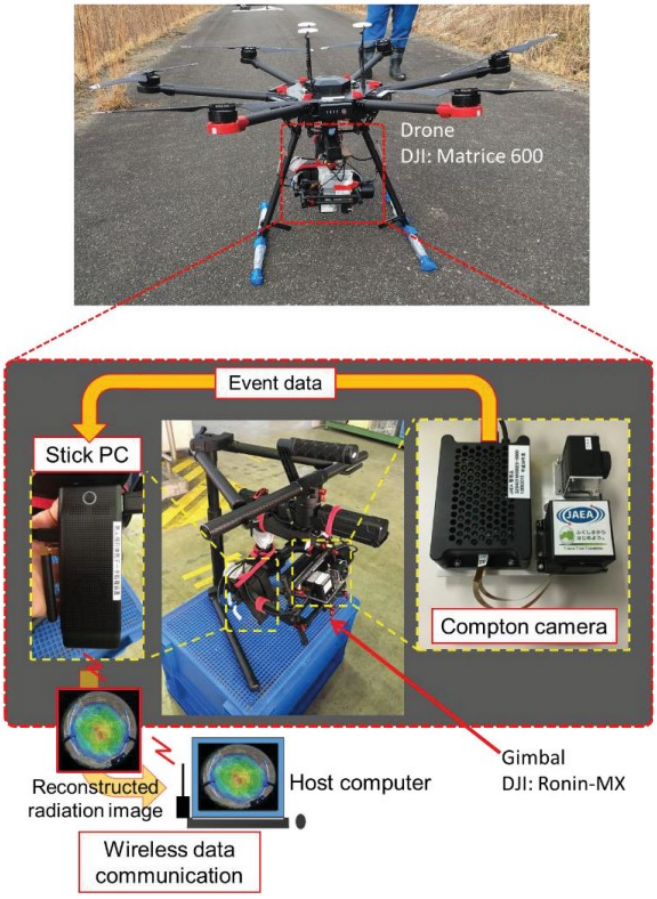

Figure 3.6: Photograph of remote radiation imaging system consisting of drone and compact Compton camera (from [62]).

Besides contaminated environments, monitoring is also conducted in medical facilities, where various low-level gamma radiation sources with a surface and/or air dose rate of just a few $\mu Sv/h$ are housed. In Muraishi et. al [63] a low-cost, high-sensitivity, omnidirectional, gamma-ray imaging Compton camera was developed and used in a nuclear medicine facility to visualize the movement of a patient injected with ^{18}F-fluorodeoxyglucose and to successfully monitor the position of the sub-MeV radioactive source.

Chapter 4

Construction of a Compton telescope for the detection of Gamma Rays

4.1 Design

A prototype Compton telescope was developed to investigate the performance of a scintillator-based absorber and scatterer in accurately localizing gamma-ray sources and measuring their energy spectra. The setup and the results of this work have been previously presented in detail in Asova et al. [64].

The prototype was designed to assess the energy resolution and detection efficiency that can be achieved with a $CeBr_3$ based detector. $CeBr_3$ crystal was used in both the scatterer and the absorber. A monolith $CeBr_3$ was chosen due to its high yield (∼68 000 ph/MeV), short light decay time (∼17 ns) and decent resolution of 4% at 662 keV [65] , [66]. $CeBr_3$ crystals are currently being under research for use in gamma-ray astronomy, including applications in nanosatellites [68] and environmental [69] monitoring. As a result, it is crucial to improve the general understanding of $CeBr_3$-based detectors and their performance characteristics. $CeBr_3$ lacks natural radioactivity, which makes it a viable option in low noise environments. A possible alternative to $CeBr_3$ would be $LaBr_3 : Ce$,which has high light yield (∼61 000 ph/MeV), high energy resolution 2.85 % ± 0.5 % at 662 keV and short decay time (26 ns) [70], but due to the natural radioactivity of lanthanum, it is not useful in low-noise environments [71] On the other hand, $LaBr_3 : Ce$'s natural radioactivity could be useful for continuous calibration and monitoring.

The choice of a monolith instead of segmented $CeBr_3$ crystal is due to the fact that monolith crystals provide high detection efficiency due to their lack of dead regions inside the crystal. Moreover, photon transport in monolithic scintillators is generally more efficient than in segmented-based detectors where the photons undergo multiple reflections and experience reduced light collection efficiency due to depth-of-interaction (DOI) dependent losses before reaching the photodetector [72].

The studied prototype investigated the properties of a scintillation detector built from one of the two available $CeBr_3$ crystals - one with dimensions 51 × 51 × 25 mm^3 and the other has 51×51×10 mm^3. In later sections the former will be referred to as "thick crystal" and to the latter as "thin crystal". In the setup one of the two crystals is coupled to a

SiPM matrix ONSEMI ARRAYC-30035-144PCB which consists of 144 pixelized avalanche photodiodes operated in Geiger mode (12x12 ARRAY of 3mm SMT sensors). A SiPM was chosen over conventional PMT-s due to the formers combination of high gain, high signal to noise ratio and low operational voltage in comparison to PMTs. The SiPM matrix and the crystal are coupled via a 3D printed housing sealed with epoxy. The matrix assembly and its housing are illustrated in Figure 4.1.

The numbered components correspond to:

- 1 - 3D printed upper casing
- 2 - $CeBr_3$ scintillator crystal
- 3 - silicone optical grease
- 4 - SiPM matrix
- 5 - Samtec 80-way connectors type QTE-040-03-F-D-A
- 6 - 3D printed lower casing
- 7 - Fasteners
- 8 - AiT AB424T-ARRAY144P Tileable 4+24 Channel Hybrid Active Base

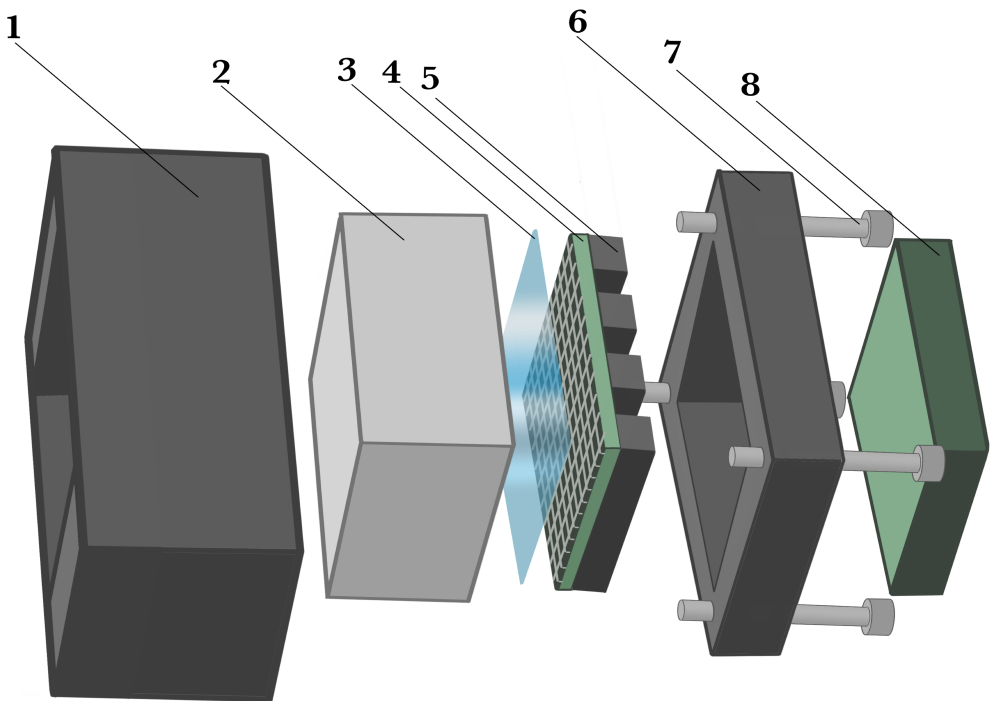

Figure 4.1: A schematic representation of the SiPM+Crystal setup

The SiPM-s are supplied with high voltage by an AiT ABPS power supply module, which also provides low voltage for for powering the frontend electronics and the amplifiers.

The output signals in each row and column of the SiPM matrix are summed through the AiT AB424T carrier, thus producing 2×12 = 24 output signals - Ax_i and Ay_i. In addition, four final outputs X^+, X^-, Y^+, Y^- are constructed electronically, which are functions of Ax_i and Ay_i in the following way:

$$X^+ = \sum_i c_i * Ax_i, \qquad X^- = \sum_i c_{12-i} * Ax_i \tag{4.1}$$

$$Y^+ = \sum_i c_i * Ay_i, \qquad Y^- = \sum_i c_{12-i} * Ay_i \tag{4.2}$$

such that $c_i + c_{12-i} = 1.0833$, leading to

$$X^+ + X^- = 1.0833 \times \sum_i Ax_i \tag{4.3}$$

$$Y^+ + Y^- = 1.0833 \times \sum_i Ay_i. \tag{4.4}$$

Consequently, each set of output signals is directed either to the 4-channel ABR4 or the 16-channel ABR16 receiver, both of which act as amplifiers of the signals and also produce analog sum signal. The output analog sum signals are then passed to a V1751 Digitizer and whenever the amplitude in any of them passes over a preset threshold (10 mV), the digitized data is forwarded to a computer. The total number of samples is set to 1024 with a sampling rate of 10^9 Samples/s. A Data Acquisition (DAQ) software stores the data in a PC and prepares it for the subsequent analysis. A schematic representation of the full setup is shown on Figure 4.2, while a more detailed description can be found in [73].

The measurements were conducted using collimated gamma-ray beams from three radioactive sources: ^{137}Cs, ^{22}Na and ^{60}Co. Collimation was achieved by means of a pinhole aperture in a thick lead block. For both the thick and thin $CeBr_3$ crystals, data was collected at three different SiPM bias voltages: 27.5 V, 28.0 V, and 28.5 V. Additionally, for the ^{137}Cs source, an extra measurement was performed at a 29.0 V bias.

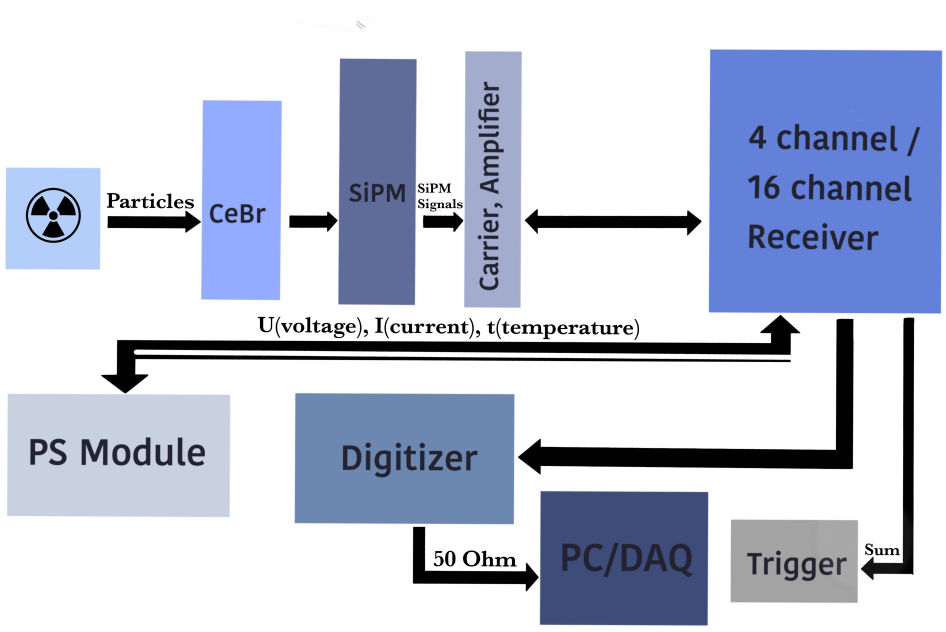

Figure 4.2: Schematics of the experimental setup The radioactive source is one of the three available (^{137}Cs, ^{22}Na, ^{60}Co).

Chapter 5

Study of the performance of a monolith CeBr3 crystal coupled to a segmented photodetector

5.1 Resolution measurement

The total charge that is reconstructed from the voltage pulse from the four outputs X^+, X^-, Y^+, Y^- is:

$$Q = \sum_i^n \frac{U(t_i)}{R} \Delta t, \tag{5.1}$$

where $U(t_i)$ are the recorded amplitudes of the signal in sample i, $\Delta t = 1$ ns is the sampling step, and $R = 50\,\Omega$ is the input impedance of the digitizer. The recorded files were processed via a custom data analysis tool based on C/C++ and the ROOT framework. From this data the spectra of the three radioactive sources is obtained. As an example, on Figures 5.1 and 5.2, the resulting spectra for ^{137}Cs are presented for the SiPMs biased with 27.5 V and with 29 V. The energy resolution of the detector is evaluated from the parameters of the spectra, with $\mu(Q)$ denoting the mean reconstructed charge of the photopeak and $\sigma(Q)$ representing its standard deviation.

The energy resolution of the detector is calculated via the formula :

$$\frac{\sigma(E)}{E} = \frac{\sigma(Q)}{\mu(Q)} \tag{5.2}$$

Figure 5.3 shows that the energy resolution as a function of the energy for each of the photopeaks in the different spectra. The plot shows that the energy resolution is at a plateau and that the value for this plateau differs depending on the crystal's dimensions. For the thin $CeBr_3$ crystal, it is at $\frac{\sigma(E)}{E} \approx 8\%$, while for the thicker one $\frac{\sigma(E)}{E} \approx 4\%$ is obtained.

Overall, it can be suggested that the energy resolution of the thick crystal is better than that of the thin crystal. This can be attributed to the fact that the thicker crystal has a greater probability of fully absorbing the incident gamma photon and more uniform

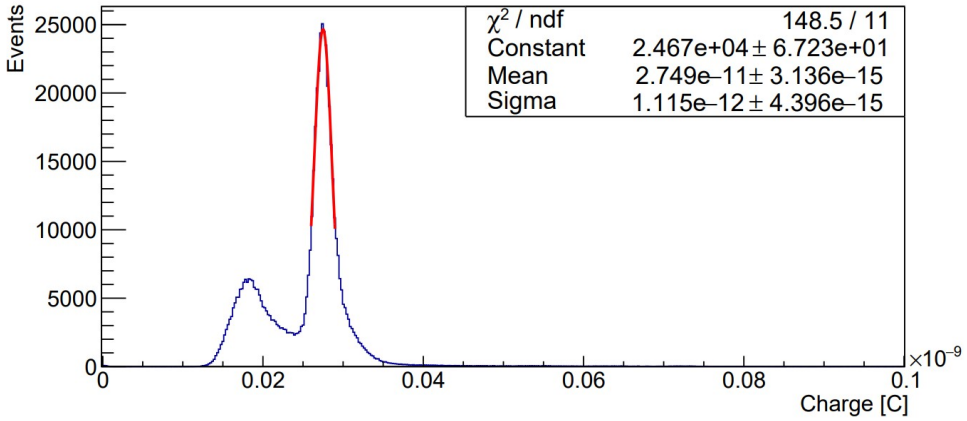

Figure 5.1: The spectrum for ^{137}Cs with 27.5 V SiPM bias voltage. Fit function of the photopeak is gaussian.

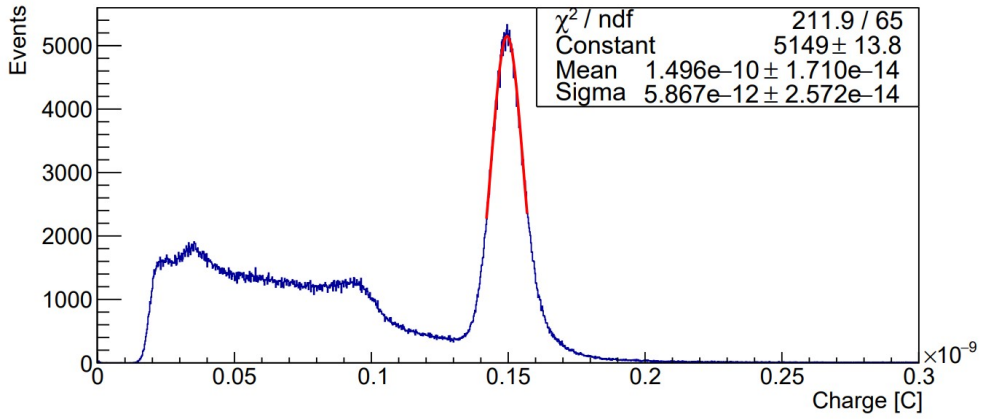

Figure 5.2: The spectrum for ^{137}Cs with 29.0 V SiPM bias voltage. Fit function of the photopeak is gaussian.

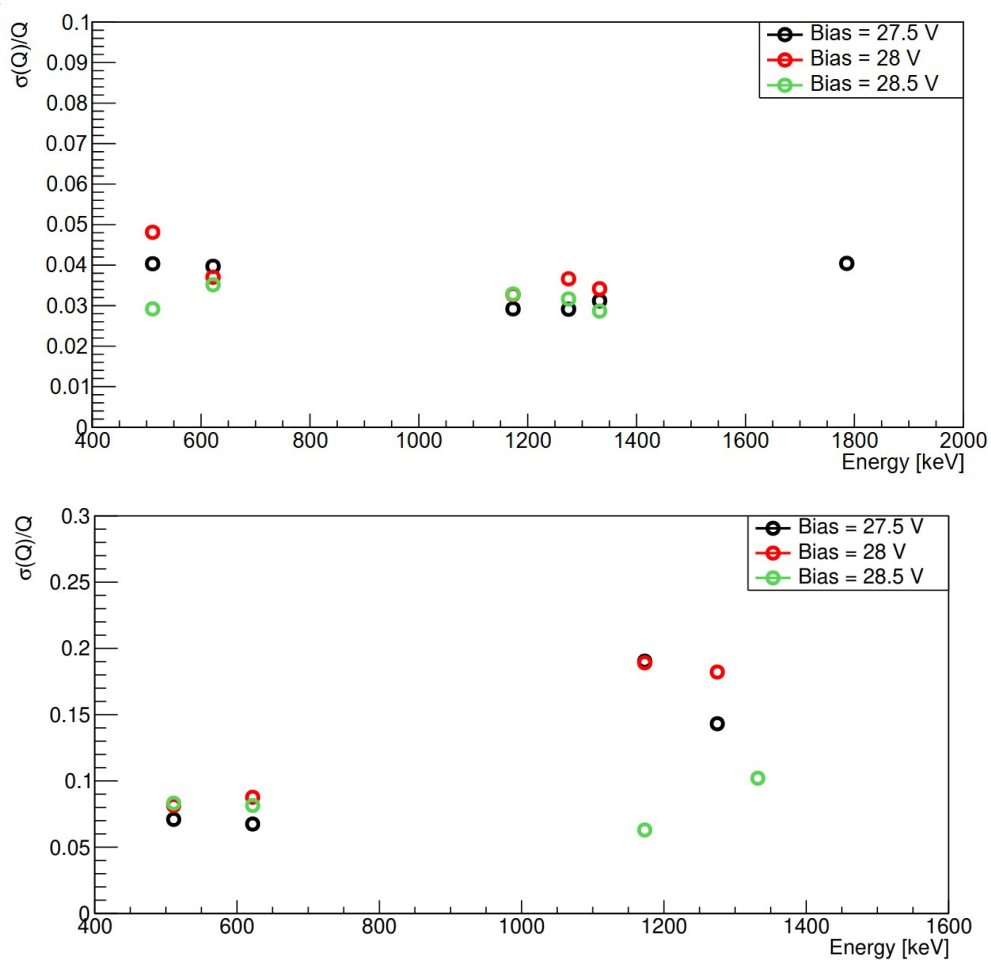

Figure 5.3: Energy resolution σ_E/E as a function of impinging gamma energy for the thin crystal (bottom) and the thick crystal (top).

distribution of the optical photons reaching the SiPM detection plane. Also, as shown in Figure 5.4, for the same isotope and bias voltage but different crystal thicknesses, the Compton edge is more pronounced in certain cases. This is attributed to Compton-scattered photons escaping the scintillator without undergoing further interactions, which results in a higher deposited energy corresponding to a photon scattering angle of 180°.

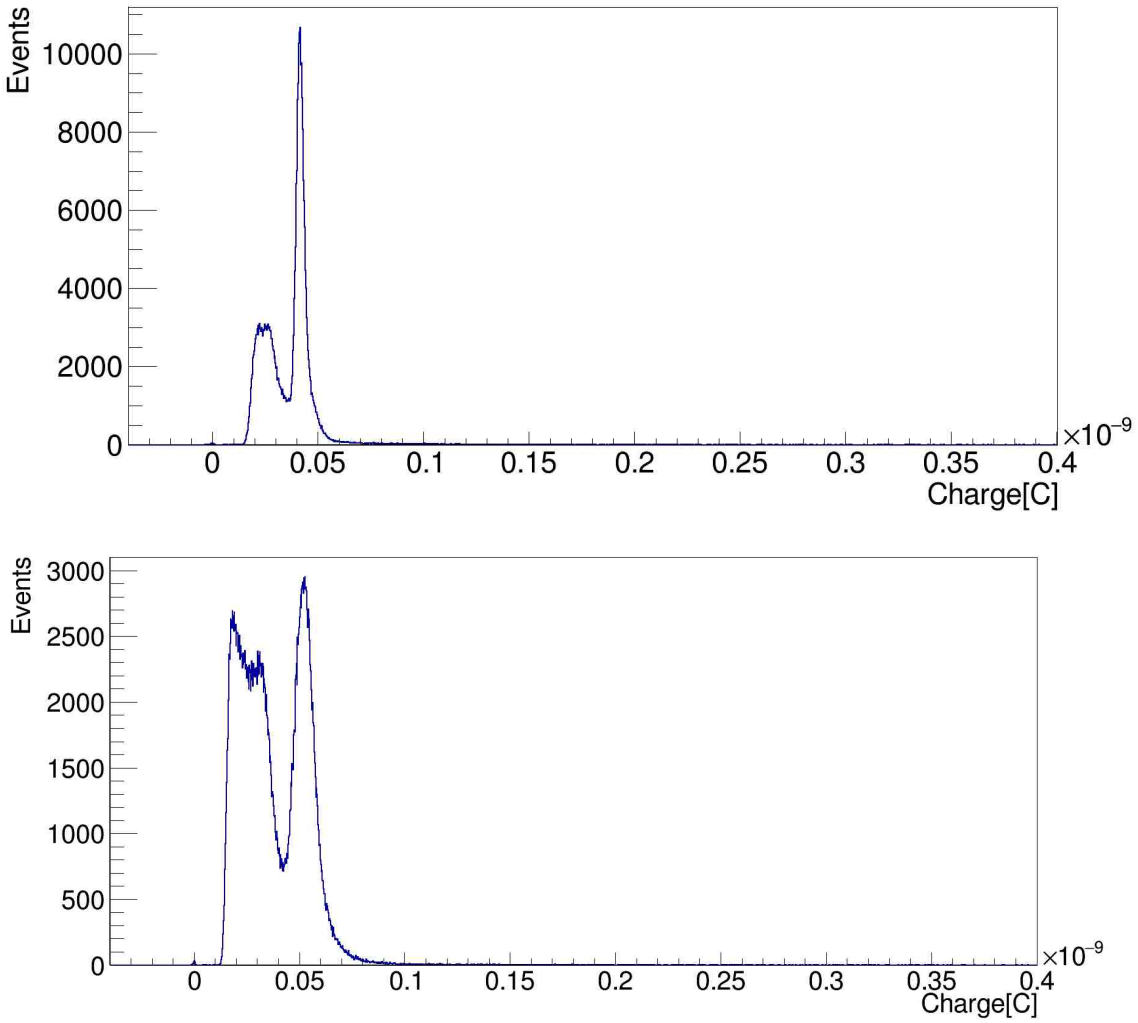

Figure 5.4: Gamma spectrum of ^{137}Cs for thick crystal (top) and the thick crystal (bottom) at 28.0 V bias. The Compton edge is more pronounced in the spectrum from the thin crystal.

All of this shows that the energy resolution of such a detector is directly affected by the properties of the crystal chosen.

5.2 Relative efficiency

The relative efficiency of the detector is defined as:

$$\varepsilon = \frac{N(1275keV)}{N(511keV)} \tag{5.3}$$

where $N(1275\ keV)$ and $N(511\ keV)$ are the number of events that consist the photopeaks of the individual energy lines of the ^{22}Na isotope. Relative count for different lines of the same spectrum was used, due to lack of a reference source to determine the absolute detector efficiency for different gamma energies.. Therefore an attempt was made to define the efficiency within a single run. Figure 5.5 shows that the relative efficiency of the thick crystal is $\varepsilon \approx 0.35$, while the efficiency of the thin one is $\varepsilon \approx 0.15$. It can be seen that the efficiency of the crystals remains mostly constant for different bias voltages, which means that it isn't dependent on parameters set by the front end electronics, but is an intrinsic quality for the crystal.

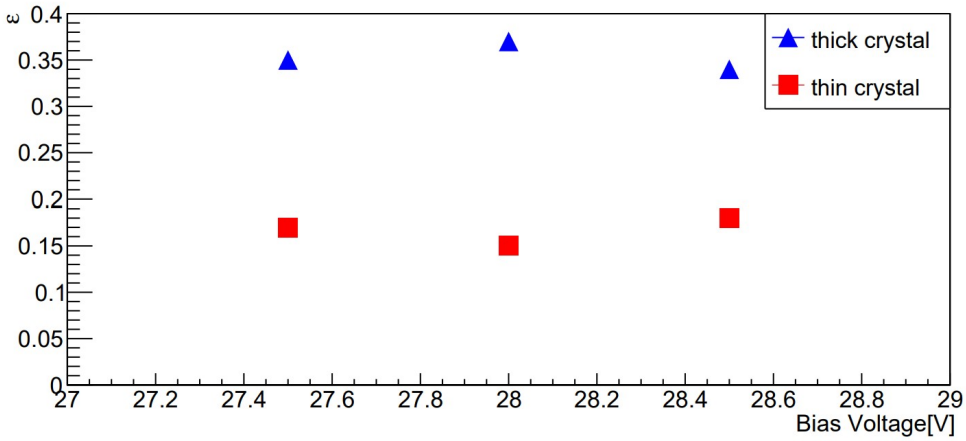

Figure 5.5: The dependence of the relative efficiency of the detector on the bias voltage.

The thin crystal exhibits lower relative efficiency because its limited thickness reduces the probability of full absorption of the 1275 keV photons, leading to more Compton scattering events and therefore fewer counts in the 1275 keV photopeak compared to the thicker crystal.

5.3 Discussion and future work

From the results stated above it can be deduced that in the design of a Compton camera, the choice of scintillator thickness plays a crucial role in determining overall performance. A thicker scintillator crystal generally offers superior energy resolution, as it increases the probability of complete energy deposition by the incident gamma photons. That would directly benefit Compton kinematic reconstruction by reducing the uncertainty in the calculated scattering angle, therefore improving image quality.

To build upon the evaluations performed in the present work, the next step would be the integration of the studied scintillator crystals into a full Compton camera. The figure below shows a prebuilt model of a Compton camera, where the thick crystal is used as an absorber and the thin crystal is used as scatterer. The back end (blue outline) of the camera will house the absorber, which will be connected to the readout system presented in the previous chapter. The front end (red outline), in which the scatterer is contained, will have its own separate readout system. This system will feature the SenSL adapter with outputs from all 144 SiPM channels, which is connected to the thick crystal in the red outline in Figure 5.6.

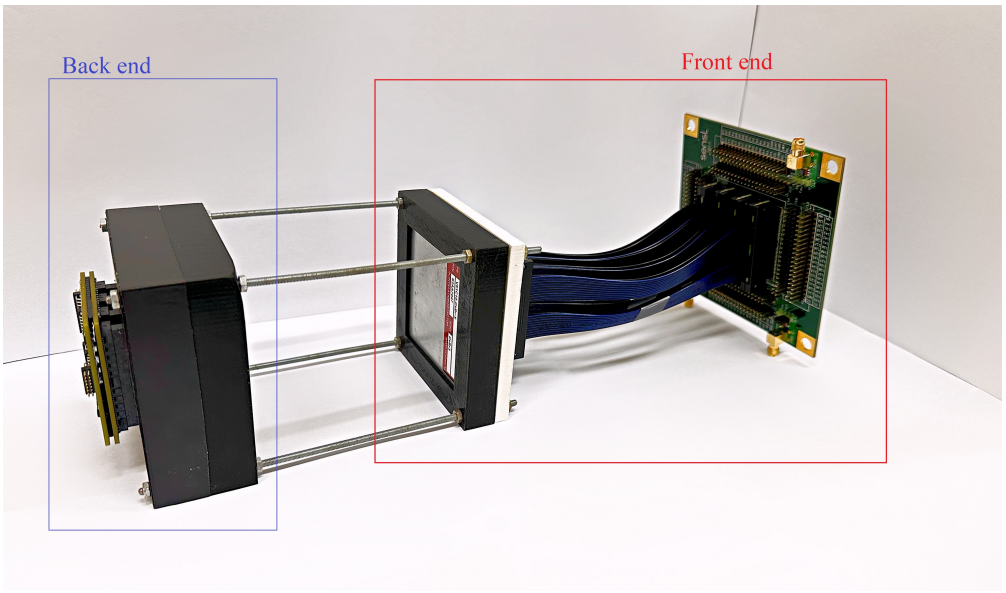

Figure 5.6: Picture of prebuilt Compton telescope. In the red outline the front end is shown, while in the blue outline is the front end.

Chapter 6

Conclusions

In the present thesis, a comprehensive study of gamma-ray detection was undertaken, beginning with an overview of the interaction mechanisms between high-energy photons and matter. Different detector technologies across various energy ranges were examined, highlighting the respective advantages and limitations of their features. Upon establishing this framework, the principles and classifications of Compton cameras were explored, including both the different types of hardware configurations and the image reconstruction algorithms that enable precise source localization. In the final sections, a prototype of a Compton camera was presented, demonstrating the dependence of energy resolution and relative efficiency on the linear dimensions of the scintillator crystal. The results of this work underscore the relationship between the physical dimensions of scintilator crystals and the detectors efficiency and resolution. This is important when constructing detection systems optimized for specific applications, where the compactness of the detector, must be balanced against performance requirements. Such considerations can improve the application of Compton cameras in fields including astrophysics, nuclear safety, and environmental monitoring.

Bibliography

[1] Davisson, C. M. (1965). Interaction of gamma-radiation with matter. In K. Siegbahn (Ed.1), Alpha-, beta- and gamma-ray spectroscopy (Vol. 1). North-Holland Publishing Company.

[2] Davisson, C. M., & Evans, R. D. (1952). Gamma-ray absorption coefficients. Reviews of Modern Physics, 24(2), 79–107. https://doi.org/10.1103/RevModPhys.24.79

[3] Pratt, R. H. (1960). Atomic photoelectric effect at high energies. Physical Review, 117(4), 1017–1028. https://doi.org/10.1103/PhysRev.117.1017

[4] Scofield, J. H. (1973). Theoretical photoionization cross sections from 1 to 1500 keV (Technical Report No. UCRL–51326). Lawrence Livermore Laboratory, University of California.

[5] Hubbell, J. H., Gimm, H. A., & Øverbø, I. (1980). Pair, triplet, and total atomic cross sections (and mass attenuation coefficients) for 1 MeV–100 GeV photons in elements Z = 1 to 100. Journal of Physical and Chemical Reference Data, 9(4), 1023–1148. https://doi.org/10.1063/1.555629

[6] Compton, A. H. (1923). A quantum theory of the scattering of X-rays by light elements. Physical Review, 21(5), 483–502. https://doi.org/10.1103/PhysRev.21.483

[7] Maximon, L. C. (1968). Simple analytic expressions for the total Born approximation cross section for pair production in a Coulomb field. Journal of Research of the National Bureau of Standards, Section B: Mathematical Sciences, 72B(1), 79–88.

[8] Fornalski, K. W. (2018). Simple empirical correction functions to cross sections of the photoelectric effect, Compton scattering, pair and triplet production for carbon radiation shields for intermediate and high photon energies. Journal of Physics Communications, 2(3), 035038. https://doi.org/10.1088/2399-6528/aab408

[9] Knoll, G. F. (2000). Radiation detection and measurement (3rd ed., p. 155). New York, NY: John Wiley & Sons.

[10] Jahoda, K., & McCammon, D. (1988). Proportional counters as low energy photon detectors. Nuclear Instruments and Methods in Physics Research Section A: Accelerators, Spectrometers, Detectors and Associated Equipment, 272(1–2), 800–813.

[11] Knoll, G. F. (2000). Radiation detection and measurement (3rd ed., pp. 159–188). New York, NY: John Wiley & Sons.

[12] Knoll, G. F. (2000). Radiation detection and measurement (3rd ed., p. 159). New York, NY: John Wiley & Sons.

[13] Fridman, A. (2008). Plasma chemistry (p. 157). Cambridge, UK: Cambridge University Press.

[14] Knoll, G. F. (2000). Radiation detection and measurement (3rd ed., p. 162). New York, NY: John Wiley & Sons.

[15] Leo, W. R. (1994). Techniques for nuclear and particle physics experiments: A how-to approach (2nd rev. ed., pp. 157–175). Berlin: Springer.

[16] Leo, W. R. (1994). Techniques for nuclear and particle physics experiments: A how-to approach (2nd rev. ed., pp. 159–164). Berlin: Springer.

[17] Leo, W. R. (1994). Techniques for nuclear and particle physics experiments: A how-to approach (2nd rev. ed., p. 162). Berlin: Springer.

[18] Leo, W. R. (1994). Techniques for nuclear and particle physics experiments: A how-to approach (2nd rev. ed., pp. 165–167). Berlin: Springer.

[19] Knoll, G. F. (2000). Radiation detection and measurement (3rd ed., pp. 231–234). New York, NY: John Wiley & Sons.

[20] Knoll, G. F. (2000). Radiation detection and measurement (3rd ed., p. 232). New York, NY: John Wiley & Sons.

[21] Knoll, G. F. (2000). Radiation detection and measurement (3rd ed., p. 233). New York, NY: John Wiley & Sons.

[22] Knoll, G. F. (2000). Radiation detection and measurement (3rd ed., pp. 265-266). New York, NY: John Wiley & Sons.

[23] Schonkeren, I. M. (1970). Photomultipliers. In H. Kater & L. J. Thompson (Eds.), Philips application book series. Eindhoven, The Netherlands: Philips.

[24] Knoll, G. F. (2000). Radiation detection and measurement (3rd ed., p. 265). New York, NY: John Wiley & Sons.

[25] Piatek, S. (2016, October 7). What is an SiPM and how does it work? Presentation, Hamamatsu Corporation & New Jersey Institute of Technology.

[26] Knoll, G. F. (2000). Radiation detection and measurement (3rd ed., pp. 353–391). New York, NY: John Wiley & Sons.

[27] Leo, W. R. (1994). Techniques for nuclear and particle physics experiments: A how-to approach (2nd rev. ed., p. 227). Berlin: Springer.

[28] Leo, W. R. (1994). Techniques for nuclear and particle physics experiments: A how-to approach (2nd rev. ed., pp. 226-227). Berlin: Springer.

[29] Leo, W. R. (1994). Techniques for nuclear and particle physics experiments: A how-to approach (2nd rev. ed., p. 239). Berlin: Springer.

[30] Knoll, G. F. (2000). Radiation detection and measurement (3rd ed., p. 405). New York, NY: John Wiley & Sons.

[31] Leo, W. R. (1994). Techniques for nuclear and particle physics experiments: A how-to approach (2nd rev. ed., pp. 59-62). Berlin: Springer.

[32] Grupen, C., & Shwartz, B. (2008). Particle detectors (2nd ed., p. 231). Cambridge, UK: Cambridge University Press.

[33] Fabjan, C. W., & Gianotti, F. (2003). Calorimetry for particle physics. Reviews of Modern Physics, 75(4), 1243–1286. https://doi.org/10.1103/RevModPhys.75.1243

[34] Kagaya, M., Katagiri, H., Kato, R., Tojo, N., Arai, Y., Tsuru, T. G., Takeda, A., & Shimazoe, K. (2023). Development of an electron-tracking Compton camera using SOI pixel sensor for sub-MeV gamma-ray observations. Proceedings of the 38th International Cosmic Ray Conference, PoS(ICRC2023), 902. https://doi.org/10.22323/1.444.0902

[35] Leo, W. R. (1994). Techniques for nuclear and particle physics experiments: A how-to approach (2nd rev. ed., pp. 151-153). Berlin: Springer.

[36] Leo, W. R. (1994). Techniques for nuclear and particle physics experiments: A how-to approach (2nd rev. ed., p. 152). Berlin: Springer.

[37] Leo, W. R. (1994). Techniques for nuclear and particle physics experiments: A how-to approach (2nd rev. ed., p. 146). Berlin: Springer.

[38] Atwood, W. B., Abdo, A. A., Ackermann, M., Althouse, W., Anderson, B., Axelsson, M., ... & The Fermi LAT Collaboration. (2009). The Large Area Telescope on the Fermi Gamma-Ray Space Telescope Mission. The Astrophysical Journal, 697(2), 1071–1102. https://doi.org/10.1088/0004-637X/697/2/1071

[39] Parajuli, R. K., Sakai, M., Parajuli, R., & Tashiro, M. (2022). Development and applications of Compton camera—A review. Sensors, 22(19), Article 7374. https://doi.org/10.3390/s22197374

[40] Daniel, G., Limousin, O., Maier, D., Meuris, A., & Carrel, F. (2020). Compton imaging reconstruction methods: A comparative performance study of direct back-projection, SOE, a new Bayesian algorithm and a new Compton inversion method applied to real data with caliste. EPJ Web of Conferences, 225, 06006. https://doi.org/10.1051/epjconf/20202250600

[41] Wilderman, S. J., Clinthorne, N. H., Fessler, J. A., & Rogers, W. L. (1998). List-mode maximum likelihood reconstruction of Compton scatter camera images in nuclear medicine. Proceedings of the 1998 IEEE Nuclear Science Symposium Conference Record, IEEE Nuclear Science Symposium and Medical Imaging Conference (Cat. No.98CH36255), 3, 1716–1720. IEEE. https://doi.org/10.1109/NSSMIC.1998.775824

[42] Andreyev, A., Sitek, A., & Celler, A. (2009). Stochastic image reconstruction method for Compton camera. 2009 IEEE Nuclear Science Symposium Conference Record (NSS/MIC), 2985–2988. IEEE. https://doi.org/10.1109/NSSMIC.2009.5401592

[43] Watanabe, S., Takeda, S., Ishikawa, S., Odaka, H., Ushio, M., Tanaka, T., Nakazawa, K., Takahashi, T., Tajima, H., Fukazawa, Y., Kuroda, Y., & Onishi, M. (2007). Development of semiconductor imaging detectors for a Si/CdTe Compton camera. Nuclear Instruments and Methods in Physics Research Section A: Accelerators, Spectrometers, Detectors and Associated Equipment, 579(2), 871–877. https://doi.org/10.1016/j.nima.2007.05.306

[44] Milbrath, B. D., Peurrung, A. J., Bliss, M., & Weber, W. J. (2008). Radiation detector materials: An overview. Journal of Materials Research, 23(10), 2561–2581. https://doi.org/10.1557/JMR.2008.0315

[45] Lee, J. H., & Lee, C. S. (2004). Studies on sensitivity, resolution, and Doppler broadening in gamma-ray imaging with pixellated semiconductor detectors. Nuclear Physics A, 746, 639–642. https://doi.org/10.1016/j.nuclphysa.2004.09.100

[46] Alnaaimi, M., 2011. Evaluation of the UCL Compton camera imaging performance. Doctoral thesis, University College London.

[47] Alnaaimi, M. A., Royle, G. J., Ghoggali, W., Banoqitah, E., Cullum, I., & Speller, R. D. (2011). Performance evaluation of a pixellated Ge Compton camera. Physics in Medicine & Biology, 56(12), 3473–3489. https://doi.org/10.1088/0031-9155/56/12/006

[48] Watanabe, T., Enomoto, R., Muraishi, H., Katagiri, H., Kagaya, M., Fukushi, M., Kano, D., Satoh, W., Takeda, T., Tanaka, M. M., Tanaka, S., Uchida, T., Wada, K., & Wakamatsu, R. (2018). Development of an omnidirectional gamma-ray imaging Compton camera for low-radiation-level environmental monitoring. Japanese Journal of Applied Physics, 57, 026401. https://doi.org/10.7567/JJAP.57.026401

[49] Katagiri, H., Satoh, W., Enomoto, R., Wakamatsu, R., Watanabe, T., Muraishi, H., Kagaya, M., Tanaka, S., Wada, K., Tanaka, M., & Uchida, T. (2018). Development of an all-sky gamma-ray Compton camera based on scintillators for high-dose environments. Journal of Nuclear Science and Technology, 55, 1172–1179. https://doi.org/10.1080/00223131.2018.1498654

[50] Zhu, Y., Qian, S., Wang, Z., Guo, H., Ma, L., Wang, Z., & Wu, Q. (2020). Scintillation properties of GAGG:Ce ceramic and single crystal. Optical Materials, 105, 109964. https://doi.org/10.1016/j.optmat.2020.109964

[51] Dimitrakopoulos, A., Michail, C., Valais, I., Fountos, G., Kandarakis, I., & Kalyvas, N. (2025). Experimental evaluation of GAGG:Ce crystalline scintillator properties under X-ray radiation. Crystals, 15(7), 590. https://doi.org/10.3390/cryst15070590

[52] Kataoka, J., Kishimoto, A., Nishiyama, T., Fujita, T., Takeuchi, K., Kato, T., Nakamori, T., Ohsuka, S., Nakamura, S., Hirayanagi, M., Adachi, S., Uchiyama, T., & Yamamoto, K. (2013). Handy Compton camera using 3D position-sensitive scintillators coupled with large-area monolithic MPPC arrays. Nuclear Instruments and Methods in Physics Research Section A: Accelerators, Spectrometers, Detectors and Associated Equipment, 732, 403–407. https://doi.org/10.1016/j.nima.2013.05.005

[53] Todd, R., Nightingale, J., & Everett, D. (1974). A proposed γ camera. Nature, 251(5471), 132–134. https://doi.org/10.1038/251132a0

[54] Shimazoe, K., Yoshino, M., Ohshima, Y., Uenomachi, M., Oogane, K., Orita, T., Takahashi, H., Kamada, K., Yoshikawa, A., & Takahashi, M. (2020). Development of simultaneous PET and Compton imaging using GAGG-SiPM based pixel detectors. Nuclear Instruments and Methods in Physics Research Section A: Accelerators, Spectrometers, Detectors and Associated Equipment, 954, 161499. https://doi.org/10.1016/j.nima.2018.10.177

[55] Polf, J. C., Avery, S., Mackin, D. S., & Beddar, S. (2015). Imaging of prompt gamma rays emitted during delivery of clinical proton beams with a Compton camera: Feasibility studies for range verification. Physics in Medicine & Biology, 60(18), 7085–7099. https://doi.org/10.1088/0031-9155/60/18/7085

[56] Schoenfelder, V., Aarts, H., Bennett, K., de Boer, H., Clear, J., Collmar, W., Connors, A., Deerenberg, A., Diehl, R., von Dordrecht, A., den Herder, J. W., Hermsen, W., Kippen, M., Kuiper, L., Lichti, G., Lockwood, J., Macri, J., McConnell, M., ... Winkler, C. (1993). Instrument description and performance of the Imaging Gamma-Ray Telescope COMPTEL aboard the Compton Gamma-Ray Observatory. The Astrophysical Journal Supplement Series, 86(3), 657–692. https://doi.org/10.1086/191794

[57] Takada, A., Takemura, T., Yoshikawa, K., Mizumura, Y., Ikeda, T., Nakamura, Y., Onozaka, K., Abe, M., Hamaguchi, K., Kubo, H., Kurosawa, S., Miuchi, K., Saito, K., Sawano, T., & Tanimori, T. (2022). First observation of the MeV gamma-ray universe with bijective imaging spectroscopy using the electron-tracking Compton telescope on board SMILE-2+. The Astrophysical Journal, 930(1). https://doi.org/10.3847/1538-4357/ac5d86

[58] De Angelis, A., Tatischeff, V., Grenier, I. A., McEnery, J., Mallamaci, M., Tavani, M., Oberlack, U., Hanlon, L., Walter, R., Argan, A., Von Ballmoos, P., Bulgarelli, A., Bykov, A., Hernanz, M., Kanbach, G., ... & e-ASTROGAM Collaboration. (2018). Science with e-ASTROGAM: A space mission for MeV–GeV gamma-ray astrophysics. Journal of High Energy Astrophysics, 19, 1–106. https://doi.org/10.1016/j.jheap.2018.08.001

[59] Gal, O., Jean, F., Laine, F., & Leveque, C. (2000). The CARTOGAM portable gamma imaging system. IEEE Transactions on Nuclear Science, 47(3), 952–956. https://doi.org/10.1109/23.856725

[60] Amgarou, K., Patoz, A., Rothan, D., & Menaa, N. (2014, October). iPIX: A new generation gamma imager for rapid and accurate localization of radioactive hotspots. Paper presented at the 12th Symposium on International Safeguards: Linking Strategy, Implementation and People, Vienna, Austria. International Atomic Energy Agency. https://inis.iaea.org/records/46081520

[61] Wahl, C. G., Kaye, W. R., Wang, W., Zhang, F., Jaworski, J. M., King, A., Boucher, Y. A., & He, Z. (2015). The Polaris-H imaging spectrometer. Nuclear Instruments and Methods in Physics Research Section A: Accelerators, Spectrometers, Detectors and Associated Equipment, 784, 377–381. https://doi.org/10.1016/j.nima.2014.12.110

[62] Sato, Y., Kawabata, K., Ozawa, S., Izumi, R., Kaburagi, M., Tanifuji, Y., Terasaka, Y., Nakamura Miyamura, H., Kawamura, T., Suzuki, T., & Torii, T. (2017). Radiation imaging system using a compact gamma-ray imager mounted on a remotely operated machine. IFAC-PapersOnLine, 50(1), 1062–1066. https://doi.org/10.1016/j.ifacol.2017.08.218

[63] Muraishi, H., Enomoto, R., Katagiri, H., Kagaya, M., Watanabe, T., Narita, N., & Kano, D. (2020). Visualization of low-level gamma radiation sources using a low-cost, high-sensitivity, omnidirectional Compton camera. Journal of Visualized Experiments, (155), e60463. https://doi.org/10.3791/60463

[64] Asova, V., Bistrev, G., Buchakchiev, V., & Kozhuharov, V. (2024). Multichannel SiPM test readout system for gamma ray measurements with monolithic inorganic CeBr3. Journal of Physics: Conference Series, 2794, 012006. https://doi.org/10.1088/1742-6596/2794/1/012006

[65] Shah, K. S., Glodo, J., Higgins, W., van Loef, E. V. D., Moses, W. W., Derenzo, S. E., & Webber, M. J. (2004). $CeBr_3$ scintillators for gamma-ray spectroscopy. IEEE Nuclear Science Symposium Conference Record, 7, 4278–4281. https://doi.org/10.1109/NSSMIC.2004.1467981

[66] Particle Data Group, Workman, R. L., Burkert, V. D., Crede, V., Klempt, E., Thoma, U., Tiator, L., Agashe, K., Aielli, G., Allanach, B. C., Amsler, C., Antonelli, M., Aschenauer, E. C., Asner, D. M., Baer, H., Banerjee, S. W., Barnett, R. M., Baudis, L., Bauer, C. W., ... Zyla, P. A. (2022). Review of particle physics. Progress of Theoretical and Experimental Physics, 2022(8), 083C01. https://doi.org/10.1093/ptep/ptac097

[67] Gostojić, A., Tatischeff, V., Kiener, J., Hamadache, C., Peyré, J., Karkour, N., Linget, D., Gibelin, L., Lafay, X., Grave, X., Dosme, N., Legay, E., Barrillon, P., & Blin, S. (2016). Characterization of $LaBr_3 : Ce$ and $CeBr_3$ calorimeter modules for 3D imaging in gamma-ray astronomy. Nuclear Instruments and Methods in Physics Research Section A: Accelerators, Spectrometers, Detectors and Associated Equipment, 832, 24–42. https://doi.org/10.1016/j.nima.2016.06.044

[68] Toneva, Zh., Ivanov, S., Georgiev, G., Kozhuharov, V., & Lalkovski, S. (2020). Study of a small scale position-sensitive scintillator detector for γ-ray spectroscopy. Journal of Instrumentation, 15, C01013. https://doi.org/10.1088/1748-0221/15/01/C01013

[69] Idoeta, R., Herranz, M., Alegría, N., & Legarda, F. (2021). Possibilities of the use of $CeBr_3$ scintillation detectors for the measurement of the content of radionuclides in samples for environmental monitoring. Applied Radiation and Isotopes, 176, 109881. https://doi.org/10.1016/j.apradiso.2021.109881

[70] van Loef, E. V. D., Dorenbos, P., van Eijk, C. W. E., Krämer, K., & Güdel, H. U. (2001). High-energy-resolution scintillator: Ce^{3+} activated $LaBr_3$. Applied Physics Letters, 79(10), 1573–1575. https://doi.org/10.1063/1.1400779

[71] Cheng, H., Sun, B.-H., Zhu, L.-H., Li, T.-X., Li, G.-S., Li, C.-B., Wu, X.-G., & Zheng, Y. (2020). Intrinsic background radiation of $LaBr_3(Ce)$ detector via coincidence measurements and simulations. Nuclear Science and Techniques, 31, 99. https://doi.org/10.1007/s41365-020-00812-8

[72] Gonzalez-Montoro, A., Gonzalez, A. J., Pourashraf, S., Miyaoka, R. S., Bruyndonckx, P., Chinn, G., Pierce, L. A. II, & Levin, C. S. (2021). Evolution of PET detectors and event positioning algorithms using monolithic scintillation crystals. IEEE Transactions on Radiation and Plasma Medical Sciences, 5(3).

[73] Asova, V., Bistrev, G., Kushleva, A., Lalkovski, S., & Vasilev, I. (2023). Multichannel SiPM test readout system for gamma ray measurements. Journal of Physics: Conference Series, 2668, 012002. https://doi.org/10.1088/1742-6596/2668/1/012002